Severe reactive astrocytes precipitate pathological hallmarks of Alzheimer's disease via $H_2O_2^-$ production

Heejung Chun [1,2,3], Hyeonjoo Im[3], You Jung Kang[4], Yunha Kim[3], Jin Hee Shin[5], Woojin Won[1,6], Jiwoon Lim[1], Yeonha Ju[1,7,8], Yongmin Mason Park[1,7,8], Sunpil Kim[1,6], Seung Eun Lee[9], Jaekwang Lee[2], Junsung Woo[2], Yujin Hwang[3], Hyesun Cho[3,10], Seonmi Jo [2,11], Jong-Hyun Park [12], Daesoo Kim [11], Doo Yeon Kim [13], Jeong-Sun Seo[10,14], Byoung Joo Gwag[5], Young Soo Kim [15], Ki Duk Park[8,12,16], Bong-Kiun Kaang [17], Hansang Cho[4,18,19], Hoon Ryu [3,20] ✉ and C. Justin Lee [1,2,6,7] ✉

Although the pathological contributions of reactive astrocytes have been implicated in Alzheimer's disease (AD), their in vivo functions remain elusive due to the lack of appropriate experimental models and precise molecular mechanisms. Here, we show the importance of astrocytic reactivity on the pathogenesis of AD using GiD, a newly developed animal model of reactive astrocytes, where the reactivity of astrocytes can be manipulated as mild (GiDm) or severe (GiDs). Mechanistically, excessive hydrogen peroxide (H_2O_2) originated from monoamine oxidase B in severe reactive astrocytes causes glial activation, tauopathy, neuronal death, brain atrophy, cognitive impairment and eventual death, which are significantly prevented by AAD-2004, a potent H_2O_2 scavenger. These $H_2O_2^-$-induced pathological features of AD in GiDs are consistently recapitulated in a three-dimensional culture AD model, virus-infected APP/PS1 mice and the brains of patients with AD. Our study identifies H_2O_2 from severe but not mild reactive astrocytes as a key determinant of neurodegeneration in AD.

Reactive astrocytes are a cellular component of gliosis in neurodegenerative diseases such as AD. They are detected at the early phases of AD even before neuronal death[1] and are found ubiquitously throughout disease progression. In general, astrocyte reactivity has been defined as an increase in intermediate filaments, such as glial fibrillary acidic protein (GFAP) and vimentin, and ramification of hypertrophic processes, the hallmark of reactive astrocytes. Mild or moderate reactive astrocytes show weak hypertrophy within a nonoverlapping individual territory without proliferation, whereas severe reactive astrocytes have a proliferating potential with strong hypertrophy within overlapping territories[2]. However, in addition to morphological changes, the scope of reactive astrocytes covers a broad spectrum of molecular and functional changes. Reactive astrocytes undergo various life cycle stages and display graded reactivity with heterogeneous gene expression, morphology and function[3]. Therefore, it is necessary to establish precise interrelationships between the morphological, molecular and functional properties of reactive astrocytes in vivo.

To assess the correlations among the properties of reactive astrocytes in vivo, an appropriate animal model is needed to properly modulate their reactivity and study its effects on neuronal function. Many studies have used various animal models to induce or block astrocyte reactivity[4]. However, these animal models had serious drawbacks that limited the interpretation of their results. For example, a genetic ablation of both GFAP and vimentin when combined with the popular AD model of APP/PS1 transgenic mice gave conflicting reports[5,6]. Another model that used ablating proliferating astrocytes in GFAP-TK mice is impractical when combined with APP/PS1 because there are virtually no proliferating reactive astrocytes in this mouse model[6,7]. In popular animal models that employed triggering of reactive astrocytes, different types of limitations have been reported[8,9]. For example, it is impossible to

distinguish astrocyte-specific effects from the effects of other brain cells in injury-, lipopolysaccharide- or Aβ-induced disease models. In cell type-specific manipulations of inflammatory signaling pathways in astrocytes, the reactivity of astrocytes cannot be fine-tuned in graded fashion to assess the reactivity-dependent effects on neurodegeneration[10]. Therefore, an appropriate animal model of reactive astrocytes is urgently needed and can be properly designed if we understand the triggering mechanisms of reactive astrocytes.

Reactive astrocytes are triggered by factors such as cytokines from degenerating neurons, purines from damaged tissues and toxins from endogenous protein aggregates and exogenous materials[4]. These not only induce astrocyte hypertrophy but also change metabolic profiles[11] and gene expression patterns[12]. Astrocytes have a high rate of cellular metabolism with more oxidative and glycolytic potentials than other cell types in the brain[13]. In AD, astrocytes take up Aβ peptides to trigger degradation pathways such as autophagy[14–16]. Autophagy is critical for the regeneration of mitochondrial networks and viability of astrocytes[17]. We recently reported that Aβ plaques stimulate the putrescine degradation pathway and activate mitochondrial monoamine oxidase B (MAO-B) to produce astrocytic GABA and trigger astrocyte hypertrophy in APP/PS1 mice[18]. In astrocytes, such an Aβ degradation pathway is expected to increase oxidative stress through the production of H_2O_2 (ref. [11]). In addition, one of the two by-products of MAO-B is H_2O_2, raising the possibility that during the degradation of Aβ, MAO-B-mediated H_2O_2 is produced in excess. Excess amounts of H_2O_2 can potentially change the properties of astrocytes both morphologically and epigenetically, as reported for other cell types[19,20]. Moreover, these alterations might be proportional to the load of metabolic demand. However, whether such degradation mechanisms influence reactivity and change the functional properties of astrocytes is unknown.

We hypothesized that toxin-triggered H_2O_2 production via metabolic degradation pathways in astrocytes can cause severe and irreversible astrocyte reactivity and neurodegeneration. In this study, we established a toxin receptor model of reactive astrocytes introduced exogenously in vivo by crossing a *GFAP-CreER^{T2}* mouse model with an inducible diphtheria toxin receptor (iDTR) mouse model, named GiD. Through this model, we found that toxin-induced excessive H_2O_2 triggers inducible nitric oxide synthase (iNOS) expression, which serves as a marker for severe reactive astrocytes and neurodegeneration. These findings were recapitulated in a three-dimensional (3D) culture model of AD, an APP/PS1 mouse model and the brains of patients with AD.

Results

Toxin-triggered reactivity of astrocytes in GiD mice. To develop an animal model of toxin-triggered reactive astrocytes, we designed a mouse model of genetically inducible diphtheria toxin receptor (DTR) targeting astrocytes by crossing *GFAP-CreER^{T2}* mice with iDTR mice (GiD)[21,22]. After tamoxifen-induced DTR expression (Extended Data Fig. 1a), astrocytes could be targeted specifically through exogenous diphtheria toxin administration. As control, we used *GFAP-CreER^{T2}* mice and named them 'Gcon' (Extended Data Fig. 1c). Gcon mice were injected with the same amount of tamoxifen and diphtheria toxin as GiD mice to control for any possible confounding effects caused by the injected drugs. Based on previous injection protocols[23], we injected diphtheria toxin intraperitoneally twice at 50 μg kg⁻¹ and performed immunohistochemistry (IHC) (Extended Data Fig. 1c). Under this protocol, the diphtheria toxin injected in iDTR mice, when crossed with other cell type-specific Cre mice, induces selective cell death of neurons, microglia and oligodendrocytes[24–27]. Remarkably, the astrocytes in GiD mice were hypertrophied, instead of dead, in several brain regions including the cortex, hippocampus, striatum and amygdala, compared to Gcon astrocytes (Extended Data Fig. 1b–f). The discrepancy between astrocytic and non-astrocytic iDTR models was

not due to a sublethal dose of diphtheria toxin because the same injection protocol in neuronal iDTR models (*Camk2α-Cre/iDTR*; CiD) caused neuronal death in CiD mice (Extended Data Fig. 1g,h). The unique ability of astrocytes to circumvent the effects of the diphtheria toxin was possibly due to the high metabolic and degradative potential of astrocytes. We discovered that diphtheria toxin enhanced the autophagy pathway both in the brain of GiD mice and in cultured astrocytes from GiD mice (Extended Data Fig. 2a–s) and the enhanced autophagy pathway critically contributed to astrocyte survival (Extended Data Fig. 1e,f). These results suggest that astrocytes respond to toxic materials by actively degrading them and changing their morphological properties.

Dose-dependent reactivity of astrocytes in GiD mice. The ability of diphtheria toxin to trigger hypertrophy instead of cell death in GiD astrocytes raises a possibility that diphtheria toxin can control the severity of reactive astrocytes in a dose-dependent fashion. After testing various injection protocols, we established two optimal conditions that trigger two distinct states of reactive astrocytes in CA1 hippocampus (Fig. 1a), which mimic the mild/moderate and severe reactive astrocytes readily observed in the APP/PS1 and brain injury models (Supplementary Fig. 1) (ref. [28]). Under the diphtheria toxin injection protocol (50 μg kg d⁻¹ for 2 d), GiD astrocytes were significantly hypertrophied 1 week after diphtheria toxin administration compared to Gcon astrocytes and returned to their normal state 1 month after diphtheria toxin administration (defined as GiDm; Fig. 1a,b). In contrast, under the injection protocol of diphtheria toxin at 12 μg kg d⁻¹ for 16 d, GiD astrocytes showed severe hypertrophy 1 month after diphtheria toxin administration (defined as GiDs; Fig. 1a,c). Based on the severity of hypertrophy, we refer to the 1-week mild condition as 'GiDm' and the 1-month severe condition as 'GiDs'. The detailed Sholl analysis of individual reactive astrocytes showed that the sum of intersects and ramification index increased significantly in GiDm and GiDs astrocytes compared to Gcon astrocytes (Fig. 1d–f). In contrast, the ending radius, which is an indicator of astrocytic territory, was not changed (Fig. 1d,g). These results indicate that the escalating hypertrophy in GiDm and GiDs astrocytes can be seen as the escalating degree of branching. Remarkably, we found that the number of 4,6-diamidino-2-phenylindole (DAPI)⁺ cells and GFAP⁺ astrocytes in the CA1 stratum radiatum were significantly increased only in GiDs astrocytes (Fig. 1h–j). The increased number of GiDs astrocytes is due to proliferation, as shown by GFAP⁺ Ki67 signals in GiDs astrocytes (Fig. 1k,l). Taken together, depending on the diphtheria toxin dosage, reactive astrocytes can be either reversible in GiDm mice or irreversible and proliferating in GiDs mice in vivo, making it possible to investigate the in vivo function of reactive astrocytes.

Severe reactive astrocytes cause $H_2O_2^-$-mediated astrocytic iNOS expression, microglial activation and nitrosative stress in GiD mice. To understand the functional consequences of reactive astrocytes in vivo, it was important to determine the neurotrophic or neurotoxic molecules released from reactive astrocytes in GiD mice. Similar to reactive astrocytes in brain injury and APP/PS1 models, we found that GiD astrocytes showed both MAO-B-mediated aberrant GABA and augmented tonic GABA release (Supplementary Fig. 2b–i), indicating that the MAO-B pathway is activated in GiD astrocytes. In addition to GABA, MAO-Bs produce H_2O_2 and increase oxidative stress in cells[29]. MAO-B-mediated oxidative stress was also detected in cultured astrocytes (Supplementary Fig. 2l,m). To directly measure the MAO-B-mediated H_2O_2 in the GiD brain in vivo, we performed microdialysis from the CA1 hippocampus followed by Amplex UltraRed H_2O_2 assay (Fig. 2a,c and Supplementary Fig. 2a). As a result, the level of H_2O_2 was significantly elevated in GiDs compared to Gcon (Fig. 2c) astrocytes, suggesting that GiDs astrocytes produce H_2O_2 in response to
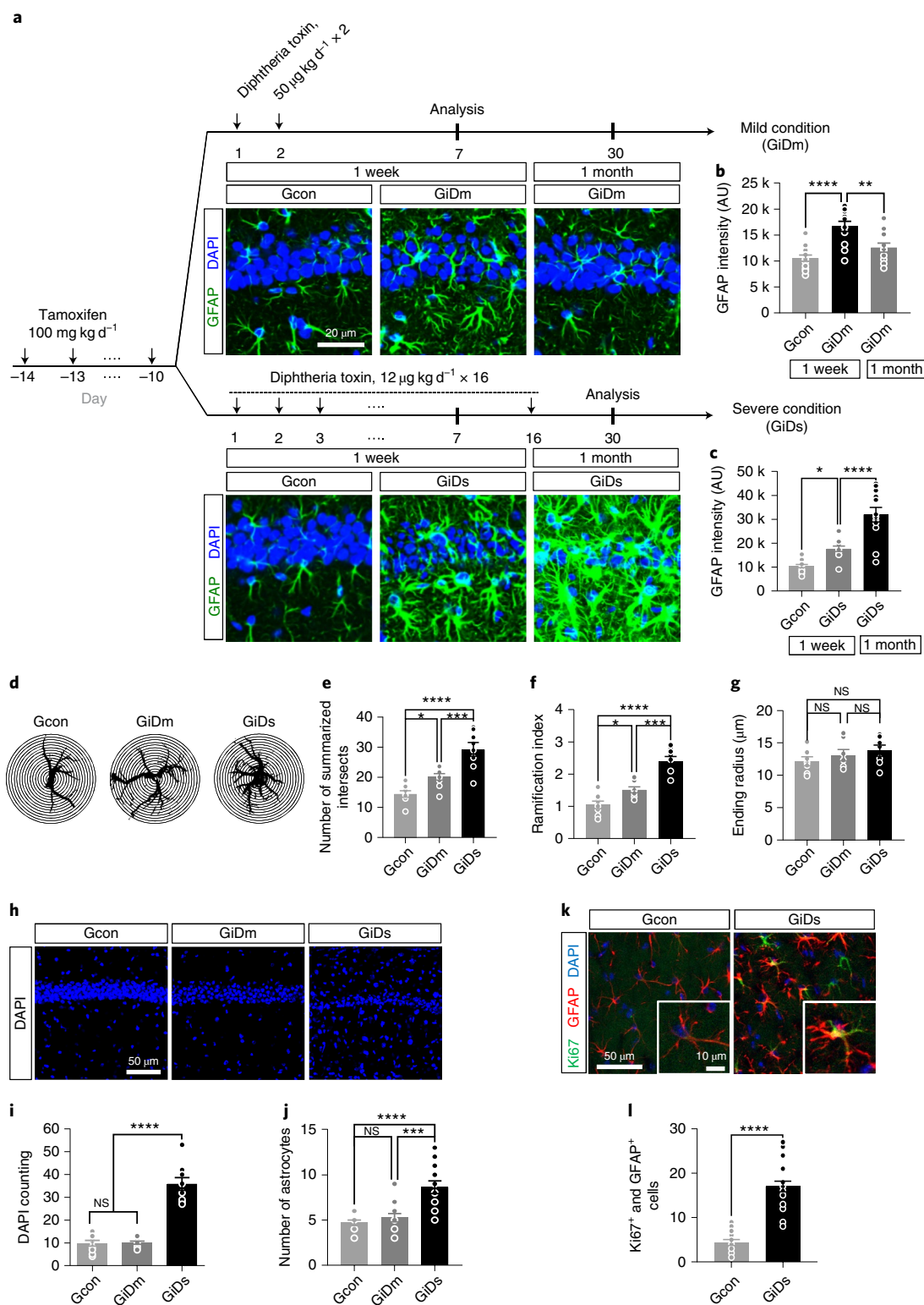
Fig. 1 | Astrocyte hypertrophy and dose-modulated reactivity in an astrocyte-specific toxin receptor model (GiD). a, Two different injection protocols of diphtheria toxin in GiD mice and immunostaining for GFAP in the CA1 region of hippocampus in mild or severe condition. **b,c**, Quantification of GFAP intensity in mild (**b**) and severe (**c**) conditions of GiD mice. **d**, Representative image for Sholl analysis of an astrocyte in the stratum radiatum from the GFAP-stained image in **a**. The interval of the concentric circles is 1 μm. **e–g**, Bar graph showing the summarized intersects (**e**), ramification index (**f**) and ending radius (**g**) by Sholl analysis from immunostained GFAP signals. **h**, DAPI staining in the CA1 hippocampus of Gcon, GiDm and GiDs astrocytes. **i,j**, Number of DAPI signals (**i**) and GFAP+ DAPI signals (**j**) in $50 \times 50\,\mu m^2$ of the striatum radiatum of Gcon, GiDm and GiDs mice. **k**, Ki67 staining in the CA1 hippocampus of Gcon and GiDs mice. **l**, Counting the number of GFAP+ Ki67 signals. Data are presented as the mean ± s.e.m. $*P < 0.05$, $**P < 0.01$, $***P < 0.001$, $****P < 0.0001$; NS, not significant. Additional statistics are provided in Supplementary Table 1.
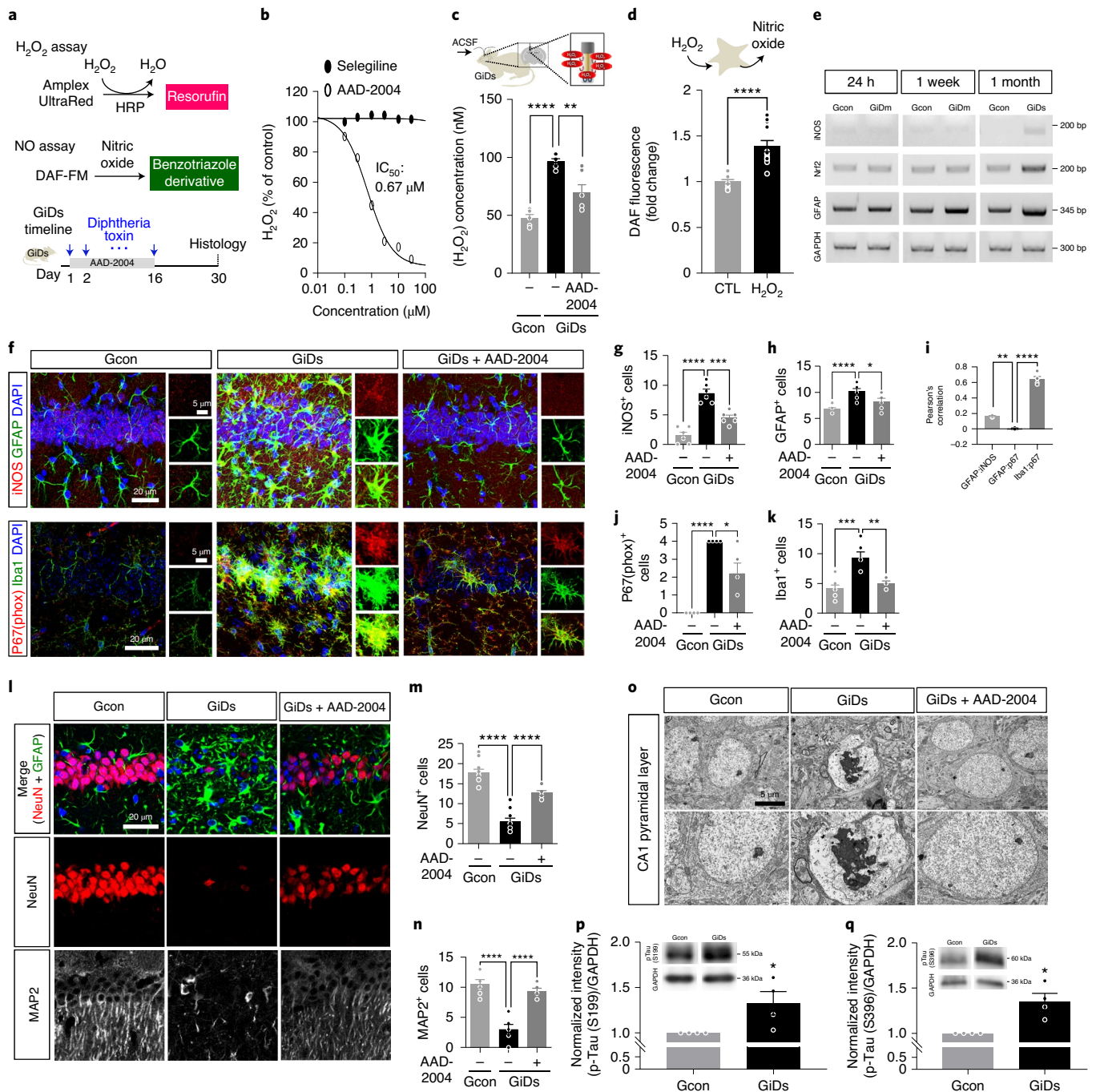
Fig. 2 | H₂O₂-mediated microglial activation, nitrosative stress, tauopathy and neurodegeneration in GiDs astrocytes. a, Schematic diagram for H_2O_2 assay using Amplex UltraRed, nitric oxide assay using the DAF-FM diacetate and GiDs timeline. **b**, In vitro H_2O_2 assay in the presence of AAD-2004 or selegiline. **c**, In vivo H_2O_2 assay after microdialysis from the CA1 region of Gcon, GiDs and AAD-2004-treated GiDs mice. **d**, In vitro nitric oxide assay in H_2O_2-treated astrocyte culture. **e**, RT–PCR analysis for *iNOS* and *Nrf2* mRNA from the hippocampus of GiDm and GiDs mice. *GAPDH* is an internal control. **f–h,j,k**, Immunostaining (**f**) and quantification of iNOS (**g**), GFAP (**h**), P67(phox) (**j**) and Iba1 (**k**) in Gcon, GiDs and AAD-2004-treated GiDs mice. **i**, Plot of Pearson's correlation coefficient between GFAP:iNOS, GFAP:P67(phox) and Iba1:P67(phox) images. **l–n**, Immunostaining (**l**) and quantification for NeuN (**m**), neuronal marker, and MAP2 (**n**), dendritic marker, in Gcon, GiDs and AAD-2004-treated GiDs mice. **o**, Transmission electron microscopy image in the CA1 pyramidal layer of Gcon, GiDs and AAD-2004-treated GiDs mice. **p,q**, Western blot analysis for p-Tau (S199) (**p**) and p-Tau (S396) (**q**) from the hippocampus of GiDs mice. Experiments were repeated more than twice. Data are presented as the mean ± s.e.m. *$P < 0.05$, **$P < 0.01$, ***$P < 0.001$, ****$P < 0.0001$. Additional statistics are provided in Supplementary Table 1.

diphtheria toxin. The in vivo increase of H_2O_2 was significantly blocked by a potent H_2O_2 scavenger, 2-hydroxy-5-[2-(4-(trifluorom ethyl-phenyl)-ethylamino]-benzoic acid (AAD-2004) (ref. [30]) (Fig. 2b,c and Supplementary Fig. 2a). These results indicate that

reactive astrocytes in GiDs mice increase the production of H_2O_2 in addition to GABA possibly via MAO-B activation.

Previous reports showed that H_2O_2 is involved in the hypertrophy of reactive astrocytes and that MAO-B mediates this

process[18,31,32]. We also found that MAO-B-mediated H_2O_2, but not GABA, is responsible for hypertrophy in GiDm (Extended Data Fig. 3a–c and Supplementary Figs. 2f,h,j,k and 5a–c). On the other hand, we showed that excessive H_2O_2 turned on nitric oxide system in cultured astrocytes (Fig. 2d), suggesting that H_2O_2 triggers the expression of nitric oxide-producing enzymes. Notably, PCR with reverse transcription (RT–PCR) analysis from the GiD hippocampus showed that inducible nitric oxide synthase, which generates a large amount of nitric oxide, was synthesized de novo in GiDs but not in GiDm or Gcon astrocytes (Fig. 2e). Excessive oxidative stress was also mirrored by upregulation of nuclear factor erythroid 2-related factor 2 in GiDs (Fig. 2e). We further examined the cellular localization of iNOS protein in the GiDs brain and observed that iNOS protein was specifically localized in GFAP+ astrocytes (Fig. 2f,g,i). In marked contrast, iNOS signals in GiDs astrocytes were significantly reduced by treatment with AAD-2004 and KDS2010, a reversible MAO-B inhibitor[33] (Fig. 2f,g and Supplementary Fig. 5b,c). These results indicate that MAO-B-dependent H_2O_2 induces iNOS expression in GiDs astrocytes. Additionally, AAD-2004 and KDS2010 treatment also blocked the increase of GFAP+ DAPI signals as well as GFAP intensity in GiDs (Fig. 2f,h and Supplementary Figs. 5b,d and 10a). Taken together, molecular cascades triggered by MAO-B and H_2O_2 in astrocytes cause severe hypertrophy, iNOS upregulation and proliferation in GiDs.

Oxidative stress is also known to play an important role in neuroinflammatory reactions including microglial activation[34]. To examine whether MAO-B activation and upregulated H_2O_2 in reactive astrocytes cause microglial activation in GiDs, we immunostained against Iba1, a marker for microglia, to observe any changes in microglial morphology. We found that Iba1-stained microglia were strongly activated as evidenced by amoeboid-like morphology near the CA1 pyramidal layer in GiDs (Fig. 2f,k). More interestingly, P67(phox) protein, a critical component of the NADPH oxidase 2 protein complex, which is the key synthetic enzyme for superoxide (O_2^-), was significantly increased in the activated microglia of GiDs (Fig. 2f,j,i), suggesting that microglia in GiDs produces O_2^-. Moreover, Iba1 and P67(phox) signals were significantly reduced in AAD-2004- and KDS2010-treated GiDs (Fig. 2f–k and Supplementary Fig. 5e–g), raising the possibility that H_2O_2 via MAO-B is the cause of global brain inflammation, including activated microglia in GiDs. Although we did not directly measure their levels, nitric oxide and O_2^- are expected to be increased in GiDs via astrocytic iNOS and microglial NADPH oxidase 2, possibly forming peroxynitrite ($ONOO^-$), a powerfully toxic oxidizing agent that can trigger the nitration of the tyrosine residues of nearby proteins. As expected, we found that the immunostained nitrotyrosine signal was significantly increased in GiDs compared to Gcon and was localized in the neuronal layer of the hippocampus. These signals were significantly blocked in AAD-2004-treated GiDs mice (Supplementary Fig. 6b–d). Taken together, these results suggest that reactive astrocytes in GiDs mice release excessive H_2O_2 and nitric oxide, which can augment nitrosative stress when combined with O_2^- from activated microglia, leading to nitration of tyrosine and eventual neurotoxicity.

Severe reactive astrocytes cause H_2O_2-mediated neurodegeneration, cognitive deficits, brain atrophy and mortality in GiDs mice. Next, we investigated the functional consequences of reactive astrocytes on neighboring neurons in the brain of GiDs mice. On the basis of previous reports[35,36], we hypothesized that reactive astrocytes would cause detrimental effects on neurons. To test this hypothesis, we performed immunostaining in GiD astrocytes with neuronal markers such as NeuN and MAP2. Remarkably, we found that immunostained NeuN and MAP2 signals were significantly disrupted in the CA1 pyramidal layer of GiDs mice, whereas such disruption was not found in GiDm mice (Fig. 2l–n and Extended

Data Fig. 3d,e). Besides the CA1 region, we observed notable disappearance of neuronal markers in other brain regions such as the cortex, striatum and amygdala in GiDs mice (Extended Data Fig. 4a–d). Interestingly, we observed an increase of neurofilament signals and decrease of neuronal DAPI size in GiDs mice, while the other neuronal markers, NeuN and MAP2, had disappeared in GiDs (Supplementary Figs. 3a–c and 4). Previous studies suggest that the reduced size of DAPI generally indicates chromatin condensation, a major feature in the nucleus of a cell undergoing necrosis or apoptosis[37]. Also, swollen, neurofilament+, dystrophic dendrites have been detected near plaques in neurodegenerative conditions[38,39]. These data suggest that the severe reactive astrocytes of GiDs mice cause neuronal damage. Because neurodegenerative mechanisms involve tauopathy in AD, we examined the phosphorylation of tau protein (p-Tau) at sites of serine 199 (S199) and serine 396/404 (S396/S404), which are the main causes of neurofibrillary tangles[40]. Interestingly, p-Tau was significantly increased in the CA1 region of GiDs mice compared to Gcon mice (Fig. 2p,q and Supplementary Fig. 6b,e–h), indicating that severe reactive astrocytes cause tauopathy in neurons. Furthermore, we observed the appearance of cleaved caspase-3 signals and terminal deoxynucleotidyl transferase dUTP nick end labeling signals in the CA1 pyramidal neurons of GiDs (Supplementary Figs. 3d,e and 6i,j). Moreover, we performed electron microscopy to see the ultrastructural signs of apoptosis in neurons of GiDs mice and observed a dramatic disruption of neuronal cell soma and chromatin condensation of neuronal nuclei, confirming apoptotic cell death in GiDs (Fig. 2o). The observed signs of neurodegeneration in GiDs mice were significantly prevented by AAD-2004 and KDS2010 treatment (Fig. 2l–o and Supplementary Figs. 5h–k and 6i,j), indicating that H_2O_2 via MAO-B is responsible for orchestrating reactive astrocyte-induced neuronal death. Taken together, we conclude that severe reactive astrocytes can cause neurodegeneration in vivo via MAO-B and H_2O_2 in this astrocyte-specific toxin receptor model, even in the absence of other endogenous toxic proteins such as Aβ.

We then assessed the behavioral consequences of the neurodegeneration observed in GiDs mice. We first examined the cognitive ability of GiDs mice by performing a passive avoidance test, which is a powerful test for hippocampus-dependent spatial memory[41]. In this experiment, spatial memory was examined by a series of retention tests (Fig. 3a). We found that GiDs mice showed a significantly reduced latency to dark room in the second retention test, compared to Gcon mice (Fig. 3b), indicating that preformed memory was impaired by diphtheria toxin-induced severe reactive astrocytes. This impairment can be interpreted as either a transient inability of memory recall or permanent memory erasure. To distinguish these possibilities, mice received another foot shock after the retention 2 test to reinforce memory (Fig. 3a). However, the preformed memory was still not retrieved and, at the same time, a new memory was not formed in retention 3 and 4 tests (Fig. 3b). Therefore, memory impairment in GiDs mice was determined as permanent memory erasure.

In addition to neurodegeneration and memory deficit, brain atrophy is one of the major features found in AD patients. Remarkably, we observed brain atrophy in GiDs mice (Fig. 3c). The brain size of GiDs mice was significantly reduced compared to Gcon mice (Fig. 3c,d). Moreover, GiDs mice showed increased mortality compared to Gcon mice (Fig. 3e). Consistent with the immunostaining data (Fig. 2 and Supplementary Fig. 5), AAD-2004 and KDS2010 treatment significantly prevented permanent memory impairment, brain atrophy and progressive death in GiDs mice (Fig. 3 and Supplementary Fig. 5l–n). These events are the major features of late-stage AD. These results suggest that brain inflammation originating from reactive astrocytes can cause the major hallmarks of AD via MAO-B and H_2O_2. In this regard, GiDs mice can be an effective animal model of dementia and AD. Furthermore, we developed
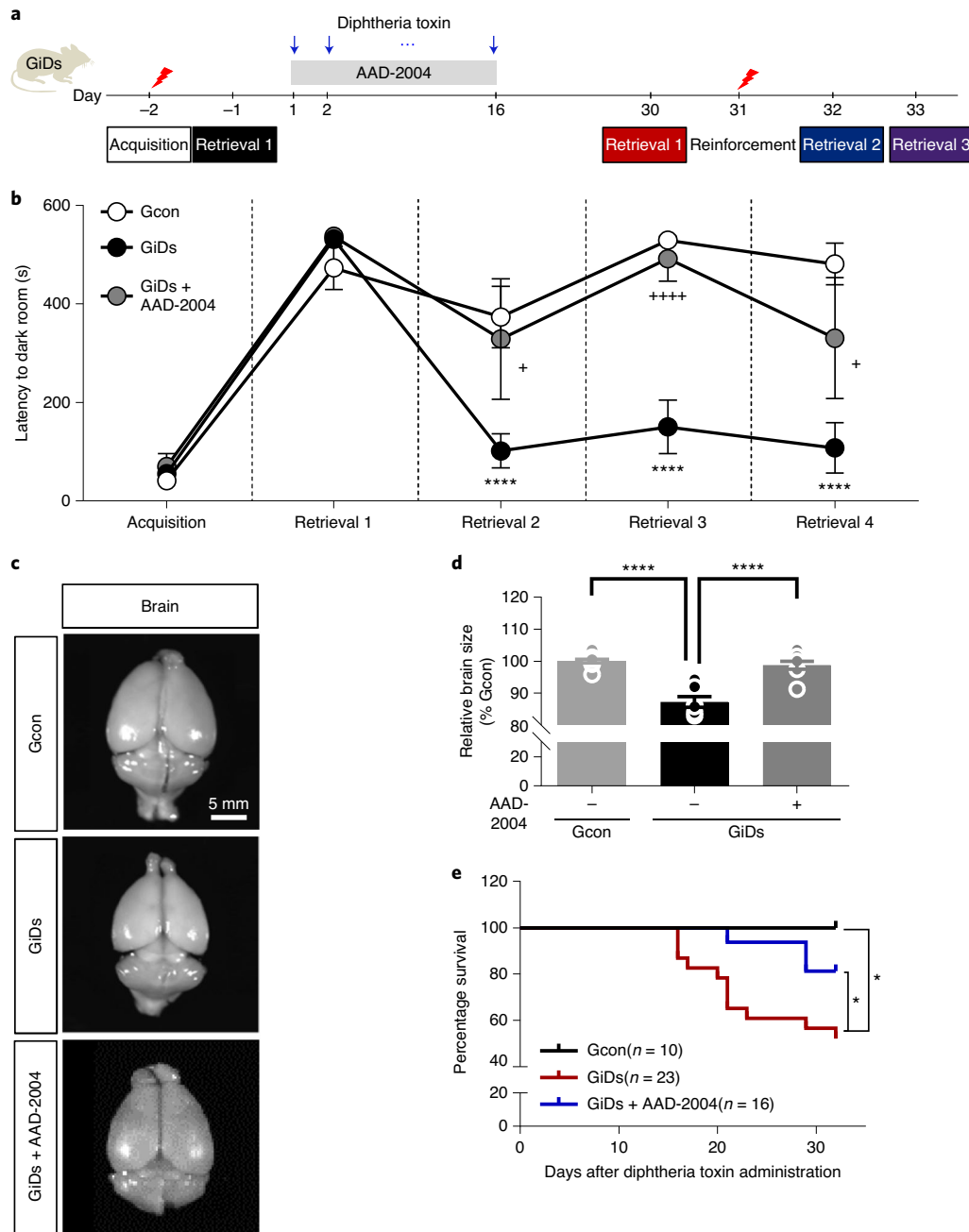
Fig. 3 | H₂O₂-mediated permanent cognitive deficits, brain atrophy and decreased survival in GiDs mice. a, Experimental protocols for the passive avoidance test. **b**, Plot of latency to dark room in the passive avoidance test in Gcon, GiDs and AAD-2004-treated GiDs mice. **c**, Representative brain images of Gcon, GiDs and AAD-2004-treated GiDs mice. **d**, Quantification of brain size measuring the diagonal of the cerebrum. **e**, Plot of survival rates in Gcon, GiDs and AAD-2004-treated GiDs mice. Data are presented as the mean ± s.e.m. $*P$ and $+P < 0.05$, $****P$ and $++++P < 0.0001$. Additional statistics are provided in Supplementary Table 1.

the focal GiD system (fGiD), which successfully recapitulated the mild and severe reactivity of astrocytes in a brain region-specific manner (fGiDm and fGiDs) (Extended Data Fig. 5a–g), raising a potential use of the GiD system in various brain diseases related to reactive astrocytes in specific brain regions.

Elevated H₂O₂ causes the hallmarks of AD in 3D culture AD model and APP/PS1 mouse. In astrocyte-specific toxin receptor models, we observed all the important hallmarks of AD even in the absence of amyloidogenesis. Moreover, we found a causal relationship between MAO-B-mediated H₂O₂ and the hallmarks of AD.

Therefore, we hypothesized that similar mechanisms might be in action in various AD models where the biological inducer of reactive astrocytes is the Aβ itself.

First, we evaluated H₂O₂-mediated reactive astrocytes, tauopathy and neurodegeneration in a recently introduced in vitro human AD brain model, which recapitulates human Aβ pathology by coculturing AD neurons and astrocytes in a 3D microfluidic platform (3D neurocyte AD)[42] (Fig. 4a,b). We measured the level of H₂O₂ and found that it significantly increased in the AD model compared to the control (Fig. 4c), which was significantly reduced in the AAD-2004-treated AD group (Fig. 4d). We simultaneously observed a
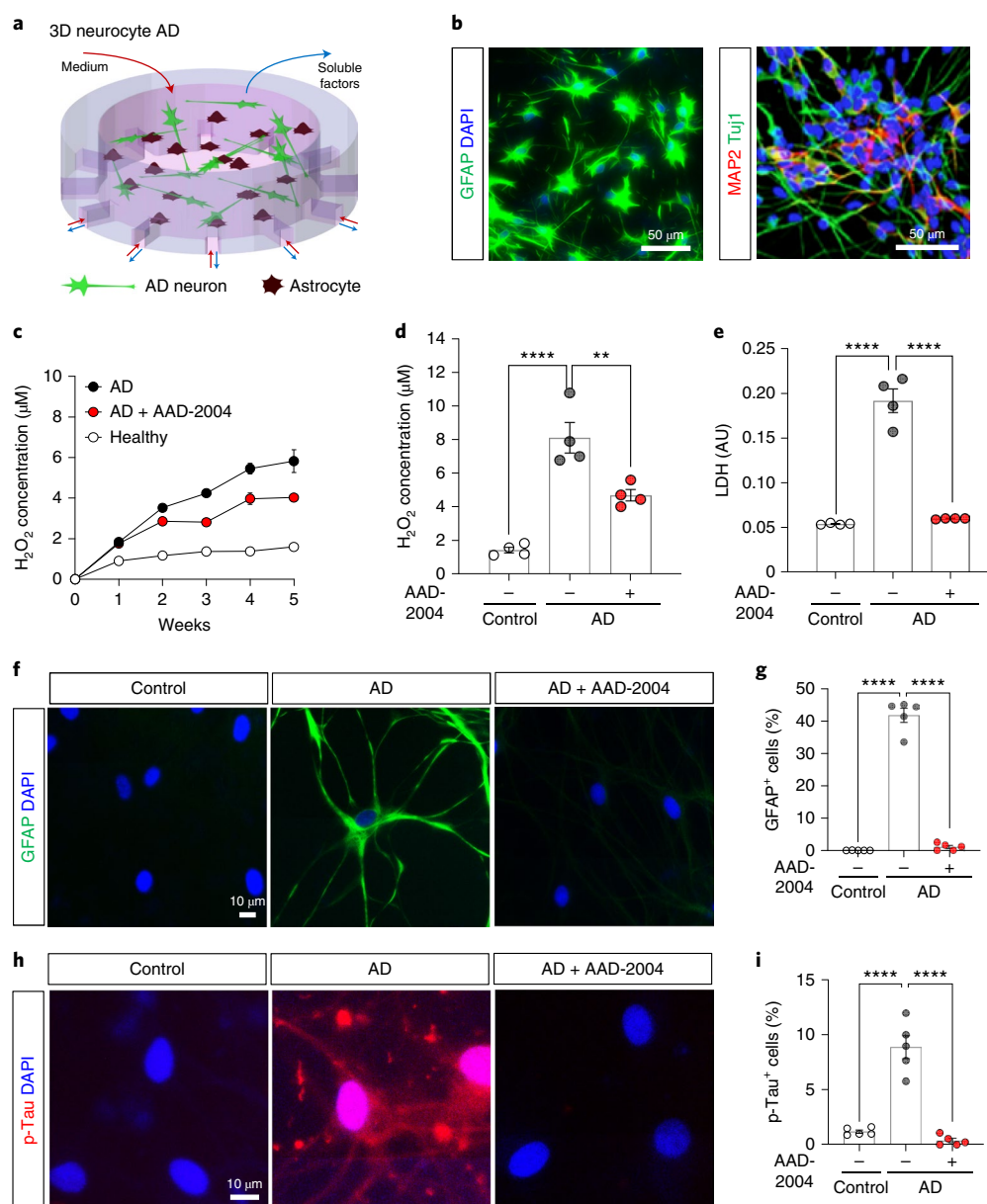
Fig. 4 | H$_2$O$_2$-mediated reactive astrocytes, tau phosphorylation and neurodegeneration in a microfluidic human AD brain model. a, Schematic illustration of multicellular layouts in a 3D microfluidic human AD brain model. **b**, Immunostaining of the AD model showing GFAP, MAP2 and Tuj1 in week 3. **c**, In vitro assessment of H$_2$O$_2$ production in the period of model development. **d**, Comparison of H$_2$O$_2$ levels during weeks 4.5–5 in healthy models, AD models and AD models treated with 100 nM of AAD-2004. **e**, Cytotoxicity assay using lactate dehydrogenase in week 5. **f,h**, Immunostaining showing GFAP (**f**) and p-Tau (S202/T205) (**h**) in week 6. **g**, Quantification of the number of cells positive for GFAP signals in week 6. **i**, Quantification of the number of cells positive for p-Tau (S202/T205) signals in week 6. Data are presented as the mean ± s.e.m. **$P < 0.01$, ****$P < 0.0001$. Additional statistics are provided in Supplementary Table 1.

significant decrease in viability as measured by lactate dehydrogenase level, increase in GFAP and increase in p-Tau (S202/T205), which were all significantly reversed by AAD-2004 treatment (Fig. 4e–i and Supplementary Fig. 7). These results strongly underpin the causal role of H$_2$O$_2$ in the Aβ-induced hypertrophy of astrocytes, tau phosphorylation and neurodegeneration.

We then evaluated the H$_2$O$_2$-mediated AD pathology in the Aβ-overproducing AD animal model, APP/PS1 mice, where numerous amyloid plaques are found and memory impairment is observed[18]. Consistently, we observed that the H$_2$O$_2$ level was increased and spatial memory ability impaired in APP/PS1 mice, which were significantly rescued by H$_2$O$_2$ scavenging through

AAD-2004 (Supplementary Fig. 8a–g). These results suggest that H$_2$O$_2$ causes memory impairment in an animal model of AD.

Focal induction of severe reactive astrocytes triggers neurodegeneration and impairs spike probability and spatial memory in APP/PS1 mice. The APP/PS1 mouse is perhaps one of the most popular animal models of AD. Unfortunately, the mouse lacks some of the important hallmarks of AD, such as nitration, tauopathy, atrophy and neuronal death[9,43]. The results from GiDs and fGiDs mice raise the possibility that the severity of reactive astrocytes could be the key factor for the failure of the APP/PS1 mouse to manifest the neurodegeneration-related hallmarks of AD. To test this possibility,
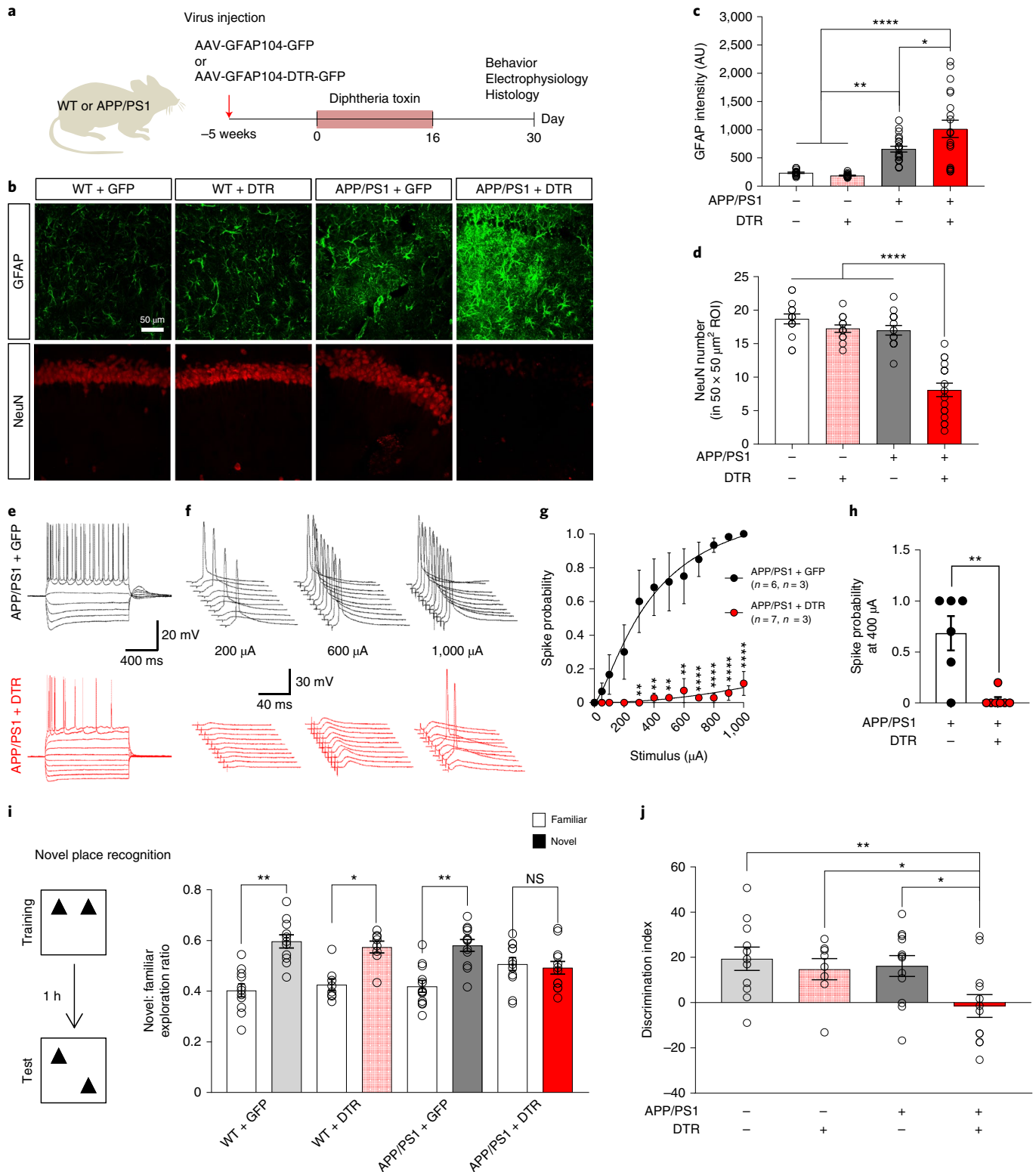
Fig. 5 | DTR-mediated increase of astrocyte reactivity and its effects on neurodegeneration, spike probability and memory ability in APP/PS1 mice.
a, Schematic diagram and experimental timeline for increasing the reactivity of astrocytes in APP/PS1 mice using the AAV-GFAP104-DTR-GFP virus.
b–**d**, Immunostaining (**b**) and quantification of GFAP (**c**) and NeuN (**d**) in virus-injected WT and APP/PS1 mice. ROI, region of interest. **e**, Representative traces of EPSPs and measurement of excitability by current injection in the CA1 pyramidal neurons of GFP- or DTR-expressing APP/PS1 mice.
f, Representative traces of evoked EPSPs and action potentials at 200, 600 and 1,000 μA electrical stimulation (0.1 Hz, 100 μs) of the Schaffer collateral pathway. **g**, Summary graph of spike probability versus stimulus intensity (0.1 Hz, 100 μs, 100–1,000 μA). **h**, Comparison of spike probability at 400 μA stimulation. **i**, Left: schematic diagram for the novel place recognition test. Right: bar graph of the exploration ratio for novel or familiar object placement in GFP/DTR-expressing WT or APP/PS1 mice. **j**, Bar graph of the discrimination index in each group. Data are presented as the mean ± s.e.m. *$P < 0.05$, **$P < 0.01$, ****$P < 0.0001$. Additional statistics are provided in Supplementary Table 1.

we injected DTR-expressing adeno-associated viruses (AAVs) under the *GFAP* promoter into the CA1 stratum radiatum of APP/PS1 mice, where it has been previously reported to contain lower levels of amyloid plaques and astrocytic reactivity than that of the dentate gyrus region at the age of 10–12 months (Fig. 5a)[18]. To prevent any confounding induction of astrocytic reactivity by the virus itself, we used a very low viral titer, previously known not to induce reactive astrocytes[44]. After diphtheria toxin administration, we observed that the reactivity of astrocytes was markedly increased in DTR-expressing APP/PS1 mice compared to DTR-expressing wild-type (WT) and green fluorescent protein (GFP)-expressing APP/PS1 mice. Importantly, we found that NeuN signals in the CA1 pyramidal layer of DTR-expressing APP/PS1 mice disappeared, whereas cleaved caspase-3 and cleaved poly (ADP-ribose) polymerase signals appeared, suggesting the acceleration of neurodegeneration by severe reactive astrocytes (Fig. 5b–dand Supplementary Fig. 9h–l). Next, we investigated whether the degenerating neurons alter their electrophysiological properties and synaptic connections. To address this issue, we performed whole-cell patch clamping in the surviving neurons (presumably NeuN− neurons) in the brain of DTR-expressing APP/PS1 mice. We examined the intrinsic membrane properties by current injections and found that these neurons had reduced excitability but still displayed action potentials (Fig. 5e). However, when we measured synaptically evoked action potential firing, we observed that these neurons showed severely impaired signal transfer (Fig. 5e–h). This phenomenon is most probably due to synaptic degeneration and/or increased tonic inhibition by severe reactive astrocytes (Supplementary Fig. 9a–e), as described previously[18]. Finally, we evaluated the memory ability of DTR-expressing APP/PS1 mice by performing the novel place recognition test, which is known to be a CA1-specific memory task[45]. We found that DTR-expressing APP/PS1 mice showed significantly impaired spatial recognition memory for novel places compared to other control groups (Fig. 5i,j). Taken together, the presence of diphtheria toxin-induced severe reactive astrocytes is sufficient to cause neurodegeneration in the CA1 and spatial memory impairment, which are otherwise lacking in APP/PS1 mice. Also, we adopted the high titer adeno-GFAP-GFP virus as a trigger for severe reactive astrocytes[46] to investigate AD features in APP/PS1 mice and consistently observed the markers of severe reactive astrocytes and neurodegeneration in a $H_2O_2^-$ and MAO-B-dependent manner (Extended Data Fig. 6a–g). These results indicate that by simply introducing severe reactive astrocytes, the missing neurodegeneration-related hallmarks of AD in APP/PS1 mice can be precipitated, suggesting that severe reactive astrocytes are sufficient for neurodegeneration.

Nitrosative stress, severe reactive astrocytes and tauopathy in human patients with AD. To verify the clinical importance of severe reactive astrocyte-mediated non-cell-autonomous

mechanisms in AD, we further determined whether the temporal cortex of patients with AD exhibited a similar pathology as shown in GiD (Supplementary Fig. 11 and Supplementary Table 2). First, we immunostained astrocytes with GFAP antibody and analyzed the morphological features of astrocytes in the brain of a patient with AD. We observed that the level of process ramification and the number of GFAP+ astrocytes were significantly increased in the patient with AD compared to a healthy individual (Fig. 6a–f). Moreover, we observed the appearance of GFAP+ Ki67 signals in the patient with AD, but not in the healthy individual, indicating the presence of proliferative severe reactive astrocytes in the brain of the patient with AD (Fig. 6g and Supplementary Fig. 10a,b). These results suggest that the reactive astrocytes in the brain of the patient with AD have morphologically similar features as the severe reactive astrocytes of GiDs mice. Next, we performed IHC with GFAP, iNOS (NOS2), Iba1 (AIF1) and P67(phox) (NCF2) antibodies and found markedly enhanced immunoreactivity for all of these targets in patients with AD compared to healthy controls (Fig. 6h–j). The iNOS signal in particular was colocalized with GFAP+ astrocytes, whereas the P67(phox) signal was colocalized with Iba1+ microglia in patients with AD (Fig. 6h). We also measured the messenger RNA levels of *GFAP*, *NOS2*, *AIF1* and *NCF2* genes; the levels of all four genes were significantly higher in patients with AD than in healthy controls (Fig. 6k). There were positive correlations between *GFAP* and *NOS2* mRNA levels and between *AIF1* and *NCF2* mRNA levels, respectively (Supplementary Fig. 10c,d). Moreover, patients with AD showed significantly increased nitrotyrosine and p-Tau (S202/T205, S199 and S396) immunoreactivities (Fig. 6l–s), which were consistent with GiDs mice and the virus-injected APP/PS1 model. These results suggest that the brains of patients with AD show the signs of severe oxidative and nitrosative stress along with the signs of severe reactive astrocytes.

Discussion

In the present study we demonstrate for the first time the causal relationship between reactive astrocytes and neurodegeneration through the fine control of astrocytic reactivity in vivo. We selectively and specifically elicited mild and severe reactive astrocytes in vivo through our toxin receptor-based animal model, GiD, and found that mild reactive astrocytes can naturally reverse its reactivity, whereas severe reactive astrocytes can cause irreversible neurodegeneration, brain atrophy and cognitive deficits, all within 30 d. This severe reactive astrocyte-induced neurodegeneration was successfully recapitulated in AAV-GFAP-DTR- and adeno-GFAP-GFP-injected APP/PS1 mice, which have been widely known to lack neurodegeneration. These results indicate that severe reactive astrocytes are sufficient for neurodegeneration. Mechanistically, toxin-responsive astrocytes activate the autophagy-mediated degradation pathway and increase MAO-B-mediated

Fig. 6 | Astrocytic hypertrophy, nitrosative stress, brain inflammation and tauopathy in the brain of patients with AD. a, Two-dimensional Sholl analysis of GFAP+ astrocytes in the superior frontal cortex of a healthy individual and patient with AD. (healthy individual or patient with AD, $n=3$; cell count, $n=30$, 10 cells per case). Astrocytes were randomly chosen for the analysis. **b**, The number of process intersections was significantly increased in GFAP+ astrocytes in the superior frontal cortex of the patient with AD. All data are the average of 30 cells (10 cells per case). **c**, The ending radius of GFAP+ astrocytes in the superior frontal cortex of the patient with AD. **d**, The sum of process intersections in GFAP+ astrocytes in the superior frontal cortex of the patient with AD. **e**, Ramification index of GFAP+ astrocytes in the superior frontal cortex of the patient with AD. All data are the average of 30 cells (10 cells per case; healthy individual ($n=3$) and patient with AD ($n=3$)). **f**, Number of GFAP+ astrocytes in the superior frontal cortex of healthy individuals and patients with AD. The y axis indicates the number of GFAP+ cells in 370 mm² of ROI. **g**, Immunostaining for Ki67 and number of GFAP− and Ki67+ cells in the brain of healthy patients and patients with AD (y axis, cell number in 10 mm² ROI). **h**, Top: immunostaining for iNOS and GFAP in the brain of healthy individuals and patients with AD. Bottom: immunostaining for P67(phox) and Iba1 in the brain of healthy individuals and patients with AD. **i**, Quantification of the number of iNOS+ and GFAP+ cells in the brain of healthy individuals and patients with AD. **j**, Quantification of the number of P67(phox)+ and Iba1+ cells in the brain of healthy individuals and patients with AD. **k**, RT–PCR analysis for *GFAP*, *AIF1*, *NOS2* and *NCF2* mRNA in the brain of healthy individuals and patients with AD. **l–s**, DAB staining and quantification for nitrotyrosine (**l,m**), p-Tau (S199) (**n,o**), p-Tau (S202/T205) (**p,q**) and p-Tau (S396) (**r,s**) in the brain of healthy individuals and patients with AD. Data are presented as the mean ± s.e.m. *$P < 0.05$, **$P < 0.01$, ***$P < 0.001$, ****$P < 0.0001$. Additional statistics are provided in Supplementary Table 1. Additional information regarding the human participants are provided in Supplementary Table 2.

H$_2$O$_2$, causing morphological hypertrophy of astrocytic processes. Notably, excessive activation of this process turns on iNOS transcription, nitrosative stress, microglial activation and tauopathy (Supplementary Fig. 11). All of these signs of reactive astrocytes and neurodegeneration were prevented by the recently developed reversible MAO-B inhibitor KDS2010 or the potent H$_2$O$_2$ scavenger
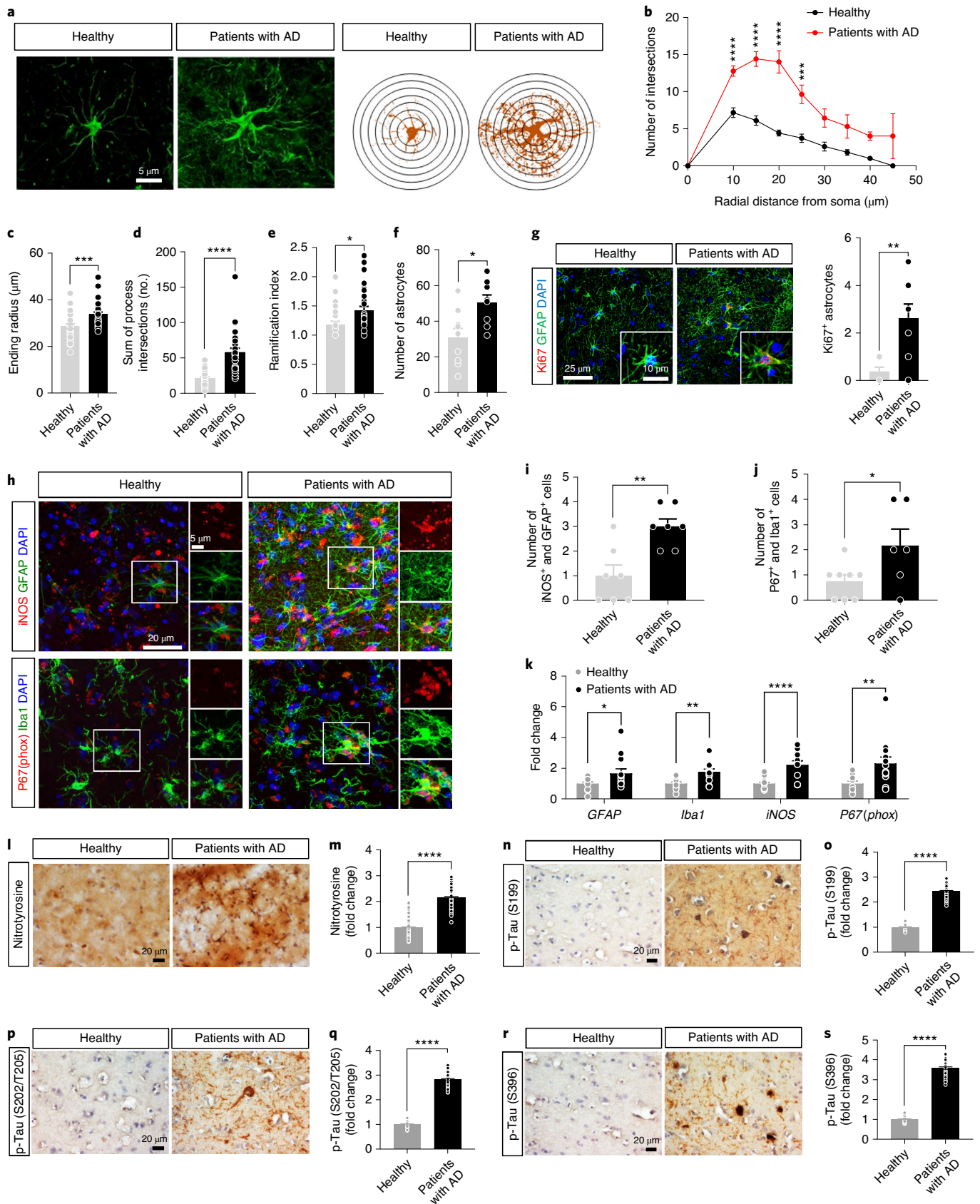
AAD-2004, indicating that severe reactive astrocytes are necessary for neurodegeneration.

Our study proposes that there is a conserved molecular pathway in reactive astrocytes found under various toxic environments such as AD. In our previous and current studies, we have demonstrated how common molecular pathways such as MAO-B-dependent putrescine degradation and GABA production pathway are shared, even though the triggering factors are different. How can differentially stimulated reactive astrocytes share the common MAO-B-GABA pathway? We suggest that the autophagic degradation pathway is commonly triggered by pathogenic molecules such as diphtheria toxin, Aβ, α-synuclein, cytokines or damaged tissue debris. More importantly, we have demonstrated how some reactive astrocytes (severe reactive astrocytes) become neurotoxic when other reactive astrocytes (mild reactive astrocytes) return to normal, even though they are sharing common mechanisms. We have discovered that MAO-B-mediated excessive H_2O_2 production is the key common molecular switch that turns on a distinct state of severe reactive astrocytes featuring iNOS and Ki67 as the molecular signature. Functionally, turned-on iNOS leads to the production of nitric oxide in severe reactive astrocytes, nitrosylation and neurodegeneration in neighboring neurons (Supplementary Fig. 11). Finally, these molecular features of severe reactive astrocytes are commonly shared in GiDs, the AD model and human AD.

Our study raises profound implications for the current theory of AD pathogenesis, providing many missing pieces to the unsolved puzzle. It provides a plausible explanation for how patients with severe AD can have continued neurodegeneration and cognitive decline even after Aβ removal by immunotherapy. It is possible that once the neurotoxic severe reactive astrocytes are turned on, irreversible neurodegeneration continues regardless of the presence or absence of an Aβ burden. We have witnessed such examples in recent failures in AD clinical trials[47,48]. Our study can also provide a plausible explanation for why many individuals lack neurodegeneration and cognitive impairment even in the presence of an Aβ burden[49]. Even in the presence of an Aβ burden, other triggering experiences such as traumatic brain injury, viral infection and posttraumatic stress disorder might be needed to transform the vulnerable brain to the AD brain via excessive oxidative stress, which subsequently transforms mild reactive astrocytes into neurotoxic severe reactive astrocytes. Future investigations are needed to explore these exciting possibilities.

Our study adds a new dimension to the existing classification of astrocytes. As we have defined previously, resting astrocytes can become either active or reactive astrocytes depending on the modality of stimulation[28]. In this study, we further categorized reactive astrocytes into mild and severe reactive astrocytes, depending on the level of hypertrophy, toxin load, reversibility and ability to damage neurons. We suggest that the heterogeneity of reactive states may come not from the diversity of triggering factors, but rather from the severity of each stimulus. Such classifications of astrocytes reinforce the idea of astrocytic diversity and their dynamic nature. The new concepts and tools we developed in this study will prove useful in gaining deeper knowledge toward the true nature and unclaimed roles of reactive astrocytes in various neurodegenerative diseases.

Online content

Any methods, additional references, Nature Research reporting summaries, source data, extended data, supplementary information, acknowledgements, peer review information; details of author contributions and competing interests; and statements of data and code availability are available at https://doi.org/10.1038/s41593-020-00735-y.

References

1. Jack, C. R. Jr. et al. Hypothetical model of dynamic biomarkers of the Alzheimer's pathological cascade. *Lancet Neurol.* **9**, 119–128 (2010).
2. Sofroniew, M. V. Molecular dissection of reactive astrogliosis and glial scar formation. *Trends Neurosci.* **32**, 638–647 (2009).
3. Anderson, M. A., Ao, Y. & Sofroniew, M. V. Heterogeneity of reactive astrocytes. *Neurosci. Lett.* **565**, 23–29 (2014).
4. Ben Haim, L., Carrillo-de Sauvage, M. A., Ceyzériat, K. & Escartin, C. Elusive roles for reactive astrocytes in neurodegenerative diseases. *Front. Cell. Neurosci.* **9**, 278 (2015).
5. Kraft, A. W. et al. Attenuating astrocyte activation accelerates plaque pathogenesis in APP/PS1 mice. *FASEB J.* **27**, 187–198 (2013).
6. Kamphuis, W. et al. GFAP and vimentin deficiency alters gene expression in astrocytes and microglia in wild-type mice and changes the transcriptional response of reactive glia in mouse model for Alzheimer's disease. *Glia* **63**, 1036–1056 (2015).
7. Sirko, S. et al. Reactive glia in the injured brain acquire stem cell properties in response to Sonic hedgehog. *Cell Stem Cell* **12**, 426–439 (2013).
8. Chun, H. & Lee, C. J. Reactive astrocytes in Alzheimer's disease: a double-edged sword. *Neurosci. Res.* **126**, 44–52 (2018).
9. Chun, H., Marriott, I., Lee, C. J. & Cho, H. Elucidating the interactive roles of glia in Alzheimer's disease using established and newly developed experimental models. *Front. Neurol.* **9**, 797 (2018).
10. Ben Haim, L. et al. The JAK/STAT3 pathway is a common inducer of astrocyte reactivity in Alzheimer's and Huntington's diseases. *J. Neurosci.* **35**, 2817–2829 (2015).
11. Allaman, I. et al. Amyloid-β aggregates cause alterations of astrocytic metabolic phenotype: impact on neuronal viability. *J. Neurosci.* **30**, 3326–3338 (2010).
12. Liddelow, S. A. et al. Neurotoxic reactive astrocytes are induced by activated microglia. *Nature* **541**, 481–487 (2017).
13. Hertz, L., Peng, L. & Dienel, G. A. Energy metabolism in astrocytes: high rate of oxidative metabolism and spatiotemporal dependence on glycolysis/glycogenolysis. *J. Cereb. Blood Flow. Metab.* **27**, 219–249 (2007).
14. Pomilio, C. et al. Glial alterations from early to late stages in a model of Alzheimer's disease: evidence of autophagy involvement in Aβ internalization. *Hippocampus* **26**, 194–210 (2016).
15. Ries, M. & Sastre, M. Mechanisms of Aβ clearance and degradation by glial cells. *Front. Aging Neurosci.* **8**, 160 (2016).
16. Wyss-Coray, T. et al. Adult mouse astrocytes degrade amyloid-β. *in vitro and in situ. Nat. Med.* **9**, 453–457 (2003).
17. Korenić, A., Andjus, P., Radenović, L. & Spasojević, I. The role of autophagy and lipolysis in survival of astrocytes under nutrient deprivation. *Neurosci. Lett.* **595**, 128–133 (2015).
18. Jo, S. et al. GABA from reactive astrocytes impairs memory in mouse models of Alzheimer's disease. *Nat. Med.* **20**, 886–896 (2014).
19. Chen, Q. M., Tu, V. C., Wu, Y. & Bahl, J. J. Hydrogen peroxide dose dependent induction of cell death or hypertrophy in cardiomyocytes. *Arch. Biochem. Biophys.* **373**, 242–248 (2000).
20. Afanas'ev, I. New nucleophilic mechanisms of ROS-dependent epigenetic modifications: comparison of aging and cancer. *Aging Dis.* **5**, 52–62 (2014).
21. Buch, T. et al. A Cre-inducible diphtheria toxin receptor mediates cell lineage ablation after toxin administration. *Nat. Methods* **2**, 419–426 (2005).
22. Park, Y. M., Chun, H., Shin, J. I. & Lee, C. J. Astrocyte specificity and coverage of hGFAP-CreERT2 [Tg(GFAP-Cre/ERT2)13Kdmc] mouse line in various brain regions. *Exp. Neurobiol.* **27**, 508–525 (2018).
23. Gropp, E. et al. Agouti-related peptide-expressing neurons are mandatory for feeding. *Nat. Neurosci.* **8**, 1289–1291 (2005).
24. Durieux, P. F. et al. D_2R striatopallidal neurons inhibit both locomotor and drug reward processes. *Nat. Neurosci.* **12**, 393–395 (2009).
25. Arruda-Carvalho, M. et al. Posttraining ablation of adult-generated olfactory granule cells degrades odor–reward memories. *J. Neurosci.* **34**, 15793–15803 (2014).
26. Parkhurst, C. N. et al. Microglia promote learning-dependent synapse formation through brain-derived neurotrophic factor. *Cell* **155**, 1596–1609 (2013).
27. Ghosh, A. et al. Targeted ablation of oligodendrocytes triggers axonal damage. *PLoS ONE* **6**, e22735 (2011).
28. Chun, H. et al. Astrocytic proBDNF and Tonic GABA distinguish active versus reactive astrocytes in hippocampus. *Exp. Neurobiol.* **27**, 155–170 (2018).
29. Maggiorani, D. et al. Monoamine oxidases, oxidative stress, and altered mitochondrial dynamics in cardiac ageing. *Oxid. Med. Cell. Longev.* **2017**, 3017947 (2017).
30. Shin, J. H. et al. Concurrent blockade of free radical and microsomal prostaglandin E synthase-1-mediated PGE_2 production improves safety and efficacy in a mouse model of amyotrophic lateral sclerosis. *J. Neurochem.* **122**, 952–961 (2012).
31. Borroni, E. et al. Sembragiline: a novel, selective monoamine oxidase type B inhibitor for the treatment of Alzheimer's disease. *J. Pharmacol. Exp. Ther.* **362**, 413–423 (2017).

32. Zhu, D. et al. Hydrogen peroxide alters membrane and cytoskeleton properties and increases intercellular connections in astrocytes. *J. Cell Sci.* **118**, 3695–3703 (2005).

33. Park, J.-H. et al. Newly developed reversible MAO-B inhibitor circumvents the shortcomings of irreversible inhibitors in Alzheimer's disease.*Sci. Adv.* **5**, eaav0316 (2019).

34. Popa-Wagner, A., Mitran, S., Sivanesan, S., Chang, E. & Buga, A.-M. ROS and brain diseases: the good, the bad, and the ugly. *Oxid. Med. Cell. Longev.* **2013**, 963520 (2013).

35. Garwood, C. J., Pooler, A. M., Atherton, J., Hanger, D. P. & Noble, W. Astrocytes are important mediators of Aβ-induced neurotoxicity and tau phosphorylation in primary culture. *Cell Death Dis.* **2**, e167 (2011).

36. Krstic, D. et al. Systemic immune challenges trigger and drive Alzheimer-like neuropathology in mice. *J. Neuroinflammation* **9**, 151 (2012).

37. Eidet, J. R., Pasovic, L., Maria, R., Jackson, C. J. & Utheim, T. P. Objective assessment of changes in nuclear morphology and cell distribution following induction of apoptosis. *Diagn. Pathol.* **9**, 92 (2014).

38. Benzing, W. C., Mufson, E. J. & Armstrong, D. M. Alzheimer's disease-like dystrophic neurites characteristically associated with senile plaques are not found within other neurodegenerative diseases unless amyloid β-protein deposition is present. *Brain Res.* **606**, 10–18 (1993).

39. Yang, D.-S. et al. Neuronal apoptosis and autophagy cross talk in aging PS/APP mice, a model of Alzheimer's disease. *Am. J. Pathol.* **173**, 665–681 (2008).

40. Augustinack, J. C., Schneider, A., Mandelkow, E.-M. & Hyman, B. T. Specific tau phosphorylation sites correlate with severity of neuronal cytopathology in Alzheimer's disease. *Acta Neuropathol.* **103**, 26–35 (2002).

41. Stephenson, R. M. & Andrew, R. J. Amnesia due to β-antagonists in a passive avoidance task in the chick. *Pharmacol. Biochem. Behav.* **15**, 597–604 (1981).

42. Park, J. et al.A 3D human triculture system modeling neurodegeneration and neuroinflammation in Alzheimer's disease.*Nat. Neurosci.* **21**, 941–951 (2018).

43. Schwab, C., Klegeris, A. & McGeer, P. L. Inflammation in transgenic mouse models of neurodegenerative disorders. *Biochim. Biophys. Acta* **1802**, 889–902 (2010).

44. Ortinski, P. I. et al. Selective induction of astrocytic gliosis generates deficits in neuronal inhibition. *Nat. Neurosci.* **13**, 584–591 (2010).

45. Haettig, J., Sun, Y., Wood, M. A. & Xu, X. Cell-type specific inactivation of hippocampal CA1 disrupts location-dependent object recognition in the mouse. *Learn. Mem.* **20**, 139–146 (2013).

46. Woo, J. et al. Functional characterization of resting and adenovirus-induced reactive astrocytes in three-dimensional culture. *Exp. Neurobiol.* **26**, 158–167 (2017).

47. Liu, P. P., Xie, Y., Meng, X.-Y. & Kang, J.-S. History and progress of hypotheses and clinical trials for Alzheimer's disease. *Signal Transduct. Target. Ther.* **4**, 29 (2019).

48. Hawkes, N. Merck ends trial of potential Alzheimer's drug verubecestat. *BMJ* **356**, j845 (2017).

49. Roostaei, T. et al. Genome-wide interaction study of brain beta-amyloid burden and cognitive impairment in Alzheimer's disease. *Mol. Psychiatry* **22**, 287–295 (2017).

Methods

Animals and housing. Mice had free access to food and water and were kept on a 12-h light–dark cycle. All animals were housed in groups of 3–5 per cage. All animal care and handling was performed according to the Institutional Animal Care and Use Committee of the Institute for Basic Science (Daejeon, Korea). *GFAP-CreER^{T2}/iDTR* and *Camk2α-Cre/iDTR* lines were maintained by crossing *iDTR* transgenic mice with *GFAP-CreER^{T2}* and *Camk2α-Cre* transgenic mice, respectively. Each line was sourced from The Jackson Laboratory (stock nos. 007900 for *iDTR* and 005359 for *Camk2α-Cre*). All experiments were done with sex- and age-matched controls.

Primary cortical astrocytes. Primary cortical astrocytes were prepared from postnatal day (P) P0–P3 C57BL/6 mice as described[50]. The cerebral cortex was dissected free of adherent meninges, minced and dissociated into single-cell suspension by trituration. Cells were grown in DMEM (Invitrogen) supplemented with 25 mM of glucose, 10% heat-inactivated horse serum, 10% heat-inactivated FCS, 2 mM of glutamine and 1,000 U ml^{-1} penicillin-streptomycin. Cultures were maintained at 37 °C in a humidified 5% CO$_2$ incubator. On the third day of culture, cells were vigorously washed with repeated pipetting and the medium was replaced to get rid of debris and other floating cell types.

Virus injection. Viruses were generated from the Korea Institute of Science and Technology (KIST) Virus Facility (http://virus.kist.re.kr). The production titer was 1.5 × 10^{12} genome copies per ml for AAV-GFAP-Cre-mCherry, AAV-GFAP104-GFP and AAV-GFAP104-DTR-GFP and 4.5 × 10^{12} genome copies per ml for adeno-GFAP-GFP. Mice were anesthetized with vaporized isoflurane and placed into stereotaxic frames (Kopf). The scalp was incised and a hole drilled into the skull above the hippocampus (anterior/posterior, −2.0 mm; medial/lateral, −1.5 or +1.5 mm from bregma). The virus was loaded into a glass needle and injected bilaterally into the hippocampal CA1 region (dorsal/ventral, −1.7 mm below the dura) at a rate of 0.2 μl min^{-1} for 10 min (total 2 μl) using a syringe pump (KD Scientific).

Drug treatment. Tamoxifen was dissolved in sunflower oil containing 10% ethanol alcohol at concentration of 20 mg ml^{-1}. Mice were treated with the tamoxifen at 100 mg kg^{-1} once per day for 5 d by intraperitoneal injection. Stock solution for diphtheria toxin was made by dissolving in distilled water at a concentration of 2 mg ml^{-1}. For the drinking experiments, selegiline (R-(−)-deprenyl hydrochloride) was dissolved in water at a concentration of 10 mg kg^{-1}. AAD-2004 (supplied by GNT Pharma) was dissolved in dimethylsulfoxide at a 500-mM concentration for the stock solution. For the working solution, stock solution was diluted in PBS at a 1-mM concentration and mice were treated at 3.3 mg kg^{-1} by intraperitoneal injection.

IHC of mouse tissue sections. Mice were deeply anesthetized with 2% avertin (20 mg g^{-1}, intraperitoneally) and perfused with 0.9% saline followed by ice-cold 4% paraformaldehyde (PFA). Excised brains were postfixed overnight at 4 °C in 4% PFA and dehydrolyzed in 30% sucrose for 48 h. Coronal hippocampal sections were cut at 30 μm in a cryostat and stored in storage solution at 4 °C. Sections from storage solution were washed in PBS and incubated for 1 h in a blocking solution (0.3% Triton X-100, 2% donkey serum in 0.1 M of PBS). Primary antibodies in blocking solution were immunostained on a shaker at 4 °C overnight. After washing in PBS 3 times, sections were incubated with corresponding fluorescent secondary antibodies for 1 h at room temperature and then washed with PBS 3 times. DAPI staining was done by adding DAPI solution (1:5,000; Pierce) during the second washing step. Finally, sections were mounted with fluorescent mounting medium (Dako) and dried. A series of fluorescent images were obtained with a Nikon A1 confocal microscope; 26-μm Z stack images in 2 μm steps were processed for Sholl analysis using the NIS-Elements (Nikon, ver. 4.50.00) and ImageJ (NIH, ver. 1.52s.) software. Primary antibodies were diluted to the following amounts: anti-GFAP 1:500; anti-Iba1 1:500; anti-GABA 1:200; anti-NeuN 1:200; anti-SMI31 1:500; and anti-Ki67 1:500. Secondary antibodies were diluted 1:500 in the blocking solution. Antibody details can be found in the Reporting Summary.

3,3′-Diaminobenzidine (DAB) staining. Tissue sections were cut at 30 μm in a cryostat blocked with blocking solution (5% BSA in 0.3% Triton X-100 in Tris-buffered saline) after 3% H$_2$O$_2$ reaction and incubated with primary antibodies at 4 °C overnight. After a secondary antibody reaction, tissue slides were further processed with the Vector ABC Kit (Vector Laboratories). DAB chromogen (Sigma-Aldrich) was used to develop the immunoreactive signals. The stained tissue slides were examined under a bright field microscope and the intensity of immunoreactivity was analyzed.

Sholl analysis. Confocal images immunostained with GFAP antibody were serially stacked and projected maximally. The maximal projection image of the GFAP signal in the stratum radiatum was adopted for analysis. The plugin of Sholl analysis applied in ImageJ automatically draws serial concentric circles at 10-μm intervals from the center of the DAPI signal to the end of the most distant process in each single astrocyte and analyzes the number of intercepts of GFAP processes in each circle and the ramification index.

In vivo propidium iodide (PI) staining. To detect dead cells, PI (4 mg kg^{-1}) was administrated into the tail vein of mice. After 5 h, mice were killed and their brain tissues were processed for IHC and confocal microscopy imaging. As a positive control, a seizure mouse model induced by kainic acid (25 mg kg^{-1}, intraperitoneally) was used.

IHC of PI-stained mouse tissue sections. Primary cultured astrocytes were cultured in a poly-D-lysine (PDL)-coated 60-mm dish and divided between PDL-coated coverslips. After cells were stabilized, putrescine dihydrochloride (180 μM; Sigma-Aldrich) and AAD-2004 (10 μM; GNT Pharma) were treated for 24 h. Then, cells were fixed with PFA (4%; Sigma-Aldrich) and glutaraldehyde (0.5%; Sigma-Aldrich) for 20 min at room temperature and washed 3 times with 0.1 M PBS for 10 min each. The samples were permeabilized with Triton X-100 (0.3%; Sigma-Aldrich) and nonspecific binding was prevented with donkey serum (10%; GeneTex) for 1.5 h at room temperature. Cells were incubated with chicken anti-GFAP (1:1,000; Merck Millipore) and guinea pig anti-GABA (1:1,000; Merck Millipore) primary antibodies overnight at 4 °C. After washing 3 times with PBS, 10 min each time, donkey anti-chicken 488 and donkey anti-guinea pig 594 secondary antibody (1:500; The Jackson Laboratories) were incubated for 1.5 h at room temperature. Cells were washed with PBS for 10 min and underwent additional incubation with DAPI (1:2,000; Pierce) for 7 min. Cells were again washed 2 times with PBS for 10 min each time and coverslips were mounted.

Western blot analysis. Western blot analyses were performed as described previously[51]. The transferred blots were incubated with the following primary antibodies at 4 °C for 24 h: anti-LC3; anti-SQSTM1/p62; anti-ACTB/β-actin and anti-TUBB3/tubulin. After washing 3 times with Tris-buffered saline with 0.05% Tween 20), the blots were incubated with the appropriate secondary antibodies conjugated to horseradish peroxidase (HRP; anti-rabbit HRP (NIF 824, Amersham Pharmacia; catalog nos. 1706515 and 1706516; Pierce) at room temperature for 2 h. Then, the blots were developed by Immobilon Western ECL solution (catalog no.WBKLS0500; Merck Millipore) and immunoreactive bands were visualized using an Image Station 4000MM (catalog no. 745280; Kodak). ACTB or TUBB3 was used as the loading control.

In vivo H$_2$O$_2$ assay. Mice were anesthetized with 2% avertin (20 μg g^{-1}) and mounted in a stereotaxic frame. After exposing the skull and drilling a hole, a CMA7 guide cannula (CMA Microdialysis) was inserted in the CA1 hippocampus (anterior/posterior, −2.0 mm; medial/lateral, 1.5 mm from bregma; dorsal/ventral, −1.2 mm). In addition, anchor screws were placed in the skull and fixed with zinc polycarboxylate dental cement. After mice recovered from anesthesia, a CMA7 microdialysis probe (membrane diameter, 0.24 mm; length, 1 mm; stainless steel shaft diameter, 0.38 mm) was implanted through the guide cannula. The probe was connected to a CMA 100 microinjection pump (CMA Microdialysis) with polyethylene (PE 50) and fluorinated ethylene propylene tubing (INSTECH). Then the probe was perfused with artificial cerebrospinal fluid (aCSF; in mM: 149 NaCl, 2.8 KCl, 1.2 MgCl2, 1.2 CaCl2 and 5.4 glucose, pH 7.4) into the inlet of the probe at a flow rate of 1.5 μl min^{-1}. Perfusates from the outlet of the tubing were automatically collected in plastic vials at 8 °C using a CMA 470 refrigerated fraction collector. Dialysates were collected at 20-min intervals for 4 h and used to measure glutamate, putrescine and GABA from the second samples. Dialysates were stored at −80 °C and then analyzed using the Amplex UltraRed assay. The concentration of H$_2$O$_2$ was measured using an Amplex UltraRed reagent according to the manufacturer's instructions. The sample from the in vivo microdialysis was mixed with Amplex UltraRed reagent and HRP in aCSF. To quantify the H$_2$O$_2$ concentrations, a 1–10 mM range of H$_2$O$_2$ was used as the standard concentration. After 30 min of enzyme reaction at 37 °C, the color change of the Amplex UltraRed reagent was quantified by measuring excitation/emission at 530/590 nm with the Infinite M200 PRO microplate reader (Tecan).

Nitric oxide measurement. Relative changes in nitric oxide concentration in astrocytes were monitored using the fluorescent nitric oxide probe DAF-FM diacetate (4-amino-5-methylamino-2′,7′-difluorofluorescein). Cells were loaded with 10 μM of DAF-FM diacetate in HEPES for 30 min at room temperature. Then, the fluorescence of DAF-FM diacetate was quantified by measuring fluorescence excitation/emission at 485/520 nm with Infinite M200 PRO microplate reader.

RT–PCR analysis. Total RNA was extracted from hippocampal lysates using the RiboEx kit (GeneAll) according to the manufacturer's recommendations. The purity and concentration of RNA was determined by measuring absorbance at 260 and 280 nm. RNA was reverse-transcribed into complementary DNA (SuperScript VILO cDNA Synthesis Kit; Invitrogen) in a total volume of 100 μl according to the manufacturer's instructions. Thermal cycler conditions are as follows: 2 min at 50 °C; 15 min at 95 °C; followed by 40 cycles of 15 s at 95 °C and 1 min at 60 °C. *GAPDH* was used as a housekeeping gene.

Electrophysiology. Mice were deeply anesthetized using vaporized isoflurane and then decapitated. After decapitation, the brain was quickly excised from the skull and submerged in ice-cold cutting solution that contained: 250 mM of

sucrose; 26 mM of $NaHCO_3$; 10 mM of D-(+)-glucose; 4 mM of $MgCl_2$; 3 mM of myo-inositol; 2.5 mM of KCl; 2 mM of sodium pyruvate; 1.25 mM of NaH_2PO_4; 0.5 mM of ascorbic acid; 0.1 mM of $CaCl_2$; and 1 mM of kynurenic acid, pH 7.4. All the solution was gassed with 95% O_2 and 5% CO_2. The hemisected brain was glued onto the stage of a vibrating microtome (PRO7N; DSK) and 300-μm-thick coronal hippocampal slices were cut and transferred to an extracellular aCSF solution: 130 mM of NaCl; 3.5 mM of KCl; 24 mM of $NaHCO_3$; 1.25 mM of NaH_2PO_4; 1.5 mM of $CaCl_2$; 1.5 mM of $MgCl_2$; and 10 mM of D-(+)- glucose, pH 7.4. Slices were incubated at room temperature for at least 1 h before recording.

Tonic GABA recording. Slices were transferred to a recording chamber that was continuously perfused with aCSF solution. The slice chamber was mounted on the stage of an upright microscope and viewed with a 60× water immersion objective (numerical aperture = 0.90) with infrared differential interference contrast optics. Cellular morphology was visualized by a complementary metal oxide semiconductor camera and the Imaging Workbench software (INDEC BioSystems, ver. 9.0.4.0.). Whole-cell recordings were made from pyramidal cell somata located in the CA1 region of the hippocampus. The holding potential was −60 mV. Pipette resistance was typically 6–8 MΩ and the pipette was filled with an internal solution consisting of: 135 mM of CsCl; 4 mM of NaCl; 0.5 mM of $CaCl_2$; 10 mM of HEPES; 5 mM of EGTA; 2 mM of Mg-ATP; 0.5 mM of Na_2-GTP; and 10 mM of QX-314, pH-adjusted to 7.2 with CsOH (278–285 mOsmol). Before measuring the tonic current, the baseline current was stabilized with D-AP5 (50 μM) and CNQX (20 μM). Electrical signals were digitized and sampled at 10-ms intervals with Digidata 1550 data acquisition system and the Multiclamp 700B Amplifier (Molecular Devices) using the pClamp10.2 software. Data were filtered at 2 kHz. The amplitude of the tonic GABA current was measured by the baseline shift after bicuculline (50 μM) administration using the Clampfit software (ver. 10.6.0.13.). The frequency and amplitude of spontaneous inhibitory postsynaptic currents before bicuculline administration was detected and measured by Mini Analysis (Synaptosoft, ver. 6.0.7.).

Evoked spike probability. Synaptic responses in pyramidal cells were evoked by 0.1 Hz stimulation of Schaffer collateral path fibers (100-ms duration; 100–1,000-mA intensity) via a constant current isolation unit. The evoked excitatory postsynaptic potentials (EPSPs) were recorded using glass pipette electrodes (6–8 MW) filled with intracellular solution containing: 120 mM of potassium gluconate; 10 mM of KCl; 1 mM of $MgCl_2$; 0.5 mM of EGTA; and 40 mM of HEPES (pH 7.2 adjusted with KOH). Spiking probability was calculated as the ratio of the number of successful (spike-generating) stimulations to the total number of stimulations. Data were collected with a MultiClamp 700B amplifier using Clampex 10 acquisition software (Molecular Devices, ver. 11.0.3.03.) and digitized with Digidata 1550. Raw data were low-pass filtered at 4 kHz and collected for off-line analysis at a sampling rate of 10 kHz using the pClamp10.2 software.

Passive avoidance behavioral test. On the first experimental day, a mouse was placed in the light chamber for the acquisition trial. After 60 s of exploration, the door separating the light and dark compartments was raised, allowing the mouse to freely enter the dark chamber. When the mouse entered a dark chamber with all 4 paws, the door immediately closed and an electric foot shock (0.5 mA, 2-s duration) was delivered through the floor grid. The mouse was then returned to the home cage and the retention trial was carried out 24 h after the acquisition trial. On the following experimental day, the mouse was placed in the light chamber again. After 60 s of exploration, the door was raised to allow the mouse to enter the dark chamber. The step-through latencies of entering the dark chamber before and after the electric shock were measured to a maximum of 538 s. In GiDs mice, we made this process form a memory by pairing an electrical foot shock with the dark chamber context, which was then checked by the retention test on the following day. After the first retention trial, we repeatedly administered the diphtheria toxin as a severe condition and tested whether the acquired memory remained or not 1 month after first diphtheria toxin injection as the second, third and fourth retention trials.

Morris water maze test. APP/PS1 mice at 10 months of age received vehicle or AAD-2004 (2.5 mg kg^{-1}, twice daily) for 1 month and were subjected to the Morris water maze to assess the acquisition and retention of spatial memory. Animals were trained to find a hidden platform (10-cm diameter) at a fixed location where the center of the platform was placed 30 cm away from the wall of the pool. The water maze was a circular 100-cm pool filled with water at 25–27 °C and made opaque by the addition of nontoxic white paint. Hidden platform training was conducted for 5 d (four trials per day, 60-s trial), wherein mice could search for a platform submerged 1.5 cm beneath the surface of the water. On the day after the hidden platform test, a probe trial was conducted where the platform was removed from the pool and mice could search for the platform for 60 s. The behavioral parameters measured were mean escape latency (hidden platform test), frequency on the platform and the percentage of time spent in the target zone and on the platform (probe test). An automated tracking system (EthoVision xt ver. 14.; Noldus) was used to monitor the animal's swimming pattern, speed and the amount of time spent in each of the four quadrants. The experimenter was blinded to genotype or treatment during the Morris water maze experiment.

Novel place recognition. Mice were brought into the test room daily for 5 consecutive days and familiarized with the experimenter's hands for 5–10 min. To encode place memory for objects, mice were placed into an open field (40 × 40 cm²; height of walls, 40 cm) with two identical objects positioned in the first and the second quadrant of the cage. Mice were allowed to freely explore the objects for 10 min in the open field. Then, mice were left undisturbed in the homecage for 1 h. To test retrieval, one of the two objects from the encoding phase was moved into the opposite empty quadrant of the open field. Then, mice had 10 min to explore the arena. After each phase, the apparatus and objects were cleaned with water containing 70% ethanol. Pilot studies ensured that the mice did not show any preference for one of the objects and/or locations. The exploration behavior of each mice was monitored by a video camera and analyzed manually by an experimenter.

Culture of human neural progenitor cells (hNPCs). ReN cell VM hNPCs were purchased from Merck Millipore. ReN cells that produce high levels of Aβ (AD hNPCs) were developed through the overexpression of a variant of the human amyloid precursor protein containing K670N/M671L (Swedish mutation) and V717I (London mutation) FAD mutations (APPSL) as published previously[52]. For the control, ReN cells were transfected with the control GFP construct (control hNPCs). Either hNPCs or AD hNPCs were plated onto the culture flask coated with 1% Matrigel (BD Biosciences) in DMEM/F-12 (Thermo Fisher Scientific) medium supplemented with 2 mg of heparin (STEMCELL Technologies), 2% (v/v) B27 neuronal supplement (Thermo Fisher Scientific), 20 mg of epidermal growth factor (Sigma-Aldrich), 20 mg of basic fibroblast growth factor (Stemgent) and 1% (v/v) penicillin-streptomycin-amphotericin-B solution (Lonza) in a CO_2 cell culture incubator. Cell culture medium was changed every 3–4 d until cells were confluent.

3D cell culture of hNPCs in the microfluidic device. We applied our 3D organotypic microfluidic model mimicking the pathological signatures of human brains from patients with AD developed by Park et al.[42] to confirm the therapeutic efficacy of AAD-2004. Briefly, ReN cells were 3D-cultured in the microfluidic device at a cell density of 2×10^6 cells per ml in 20% Matrigel diluted with DMEM/F-12 differentiation medium supplemented with 2 mg of heparin, 2% (v/v) B27 neuronal supplement and 1% (v/v) penicillin-streptomycin solution without growth factors. The microfluidic devices were incubated in a CO_2 cell culture incubator; one half volume of the differentiation medium was replaced every 3.5 d until the cells were fully differentiated into neurons and astrocytes (approximately 3 weeks). We did not observe other cell types, such as microglia, in this 3D neurocyte AD model. After 4 weeks of incubation, cells were treated with 100 nM of AAD-2004 diluted in the differentiation medium.

Immunostaining on the microfluidic device. For immunostaining, 3D-cultured cells in the device were rinsed with Dulbecco's PBS twice and fixed with 4% PFA (Electron Microscopy Sciences) for 30 min at room temperature. Cells were then washed with Dulbecco's PBS twice and permeabilized through incubation in 0.1% Triton X-100 in PBS with 0.1% Tween 20) for 15 min at room temperature. Nonspecific binding was blocked through incubation in 3% human serum albumin in PBS with 0.1% Tween 20 for 2 h at room temperature. Afterwards, cells were washed five times with PBS with 0.1% Tween 20 and incubated with the following antibodies (and dilutions in PBS with 0.1% Tween 20) for 24 h: anti-p-Tau (S202/T205) antibody (1:100); anti-GFAP antibody (1:200); and anti-Tuj1 antibody (1:200). After secondary antibody reaction, the devices were washed seven times with PBS with 0.1% Tween 20 and examined under a fluorescence microscope. The intensity of immunoreactivity was analyzed using NIS-Elements software.

IHC of human brain tissues. To detect nitrotyrosine and p-Tau protein in human postmortem brain tissues, we performed IHC as described previously[18]. Paraffin-embedded tissues from the coronal plane were sectioned at 10–20 μm. Tissue sections were blocked with blocking solution after 3% H_2O_2 reaction and incubated with nitrotyrosine (1:500), p-Tau (S202/T205; AT-8) (1:200), p-Tau (S199) (1:200) and p-Tau (S396; PHF-1) (1:200) for 24 h. After reaction with secondary antibodies, tissue slides were further processed with the Vector ABC Kit. DAB chromogen was used to develop the immunoreactive signals. The stained tissue slides were examined under a bright field microscope and the intensity of immunoreactivity was analyzed using the Multi Gauge software (FUJIFILM, ver. 2.0.).

Statistics and reproducibility. All experiments in this study are representative of at least two biological replicates (mice or cell culture preparations) except for Extended Data Fig. 2b–d (these are examined once). For the GiD and APP/PS1 mice, mice with the required genotypes were randomly assigned to the experimental groups and treated in the same way. Astrocytes culture preparations from mouse pups were randomly assigned to the experimental groups. Data distribution was assumed to be normal but this was not formally tested. Data are presented as the mean ± s.e.m. All statistical analyses were performed using Prism v.8.4.3 (GraphPad Software); an unpaired, two-tailed Student's *t*-test was used to compare two groups (except for the data analysis in the following cases: a paired, two-tailed *t*-test was used in Figs. 2q and 5i and Extended Data Fig. 2p,s; a paired,

one-tailed *t*-test was used in Fig. 2p and Extended Data Fig. 2m; an unpaired, one-tailed *t*-test was used in Extended Data Fig. 1f). A one-way analysis of variance (ANOVA) with Tukey's multiple comparisons test was used to compare more than two groups as indicated in the figure legends. A two-way ANOVA with Tukey's multiple comparisons test was used to compare groups having two independent variables. A log-rank (Mantel–Cox) test was used to test the difference in survival rate. Statistical differences were considered significant when $P < 0.05$ and are indicated in the figures or figure legends. Simple linear regression analysis was used to display regression lines and calculate Pearson's correlation coefficients. No statistical methods were used to predetermine sample sizes but sample sizes are similar to those reported in previous publications. Additional statistics are provided in Supplementary Table 1 and have been deposited in a public repository.

Reporting Summary. Further information on research design is available in the Nature Research Reporting Summary linked to this article.

Data availability
The datasets generated and/or analyzed during the current study are available in the Mendeley data repository (https://data.mendeley.com/) with DOI https://doi.org/10.17632/8mf35ntz9z.1. The datasets generated for the supplementary figures are available from the corresponding author upon reasonable request. Source data are provided with this paper.

References
50. Lee, C. J. et al. Astrocytic control of synaptic NMDA receptors. *J. Physiol.* **581**, 1057–1081 (2007).
51. Kim, Y. et al. *Uvrag* targeting by *Mir125a* and *Mir351* modulates autophagy associated with *Ewsr1* deficiency. *Autophagy* **11**, 796–811 (2015).
52. Choi, S. H. et al. A three-dimensional human neural cell culture model of Alzheimer's disease. *Nature* **515**, 274–278 (2014).

Competing interests
The authors declare no competing interests.

Additional information
Extended data is available for this paper at https://doi.org/10.1038/s41593-020-00735-y.

Supplementary information is available for this paper at https://doi.org/10.1038/s41593-020-00735-y.

Correspondence and requests for materials should be addressed to H.R. or C.J.L.

Peer review information *Nature Neuroscience* thanks the anonymous reviewers for their contribution to the peer review of this work.

**Reprints and permissions information** is available at www.nature.com/reprints.
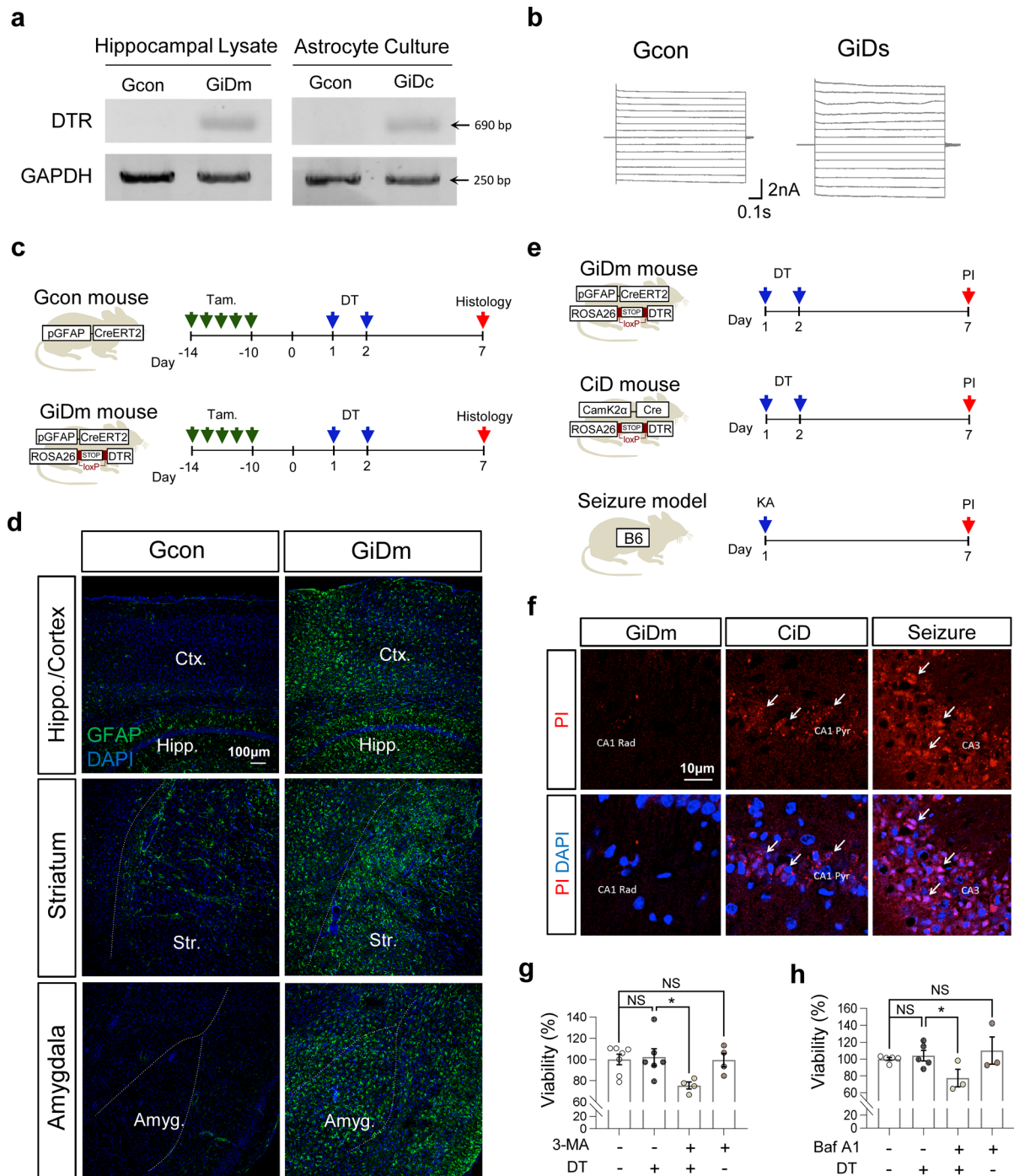
Extended Data Fig. 1 | Validation and characterization of GiD system. a, (left) RT-PCR analysis of diphtheria toxin receptor(DTR) in hippocampus of Gcon and GiDm. (right) RT-PCR analysis of DTR in cultured astrocytes from Gcon and GiD (GiDc). GAPDH, internal control. Experiments were repeated more than twice. **b**, Measuring passive conductance in astrocytes of Gcon and GiDs. **c**, Experimental procedures of GiD mice, which GFAP-CreERT2 crossed with iDTR mice. Tam, tamoxifen, 100 mg/kg/day, 5 days; DT, 50 μg/kg/day, 2 days. **d**, GFAP immunostaining in brain regions of frontal lobe containing cortex, hippocampus, striatum and amygdala of Gcon and GiD mice. Ctx, cortex; Hipp, hippocampus; Str, striatum; Amyg, amygdala. **e**, Experimental procedures for PI staining in GiDm, CiD mice and KA-injected seizure model mice. DT, 50 μg/kg/day, 2 days; KA, kainic acid, 25 mg/kg. **f**, PI staining in GiDm, CiD and seizure model mice. **g**, **h**, MTT assay in DT-treated GiD astrocyte. DT, 1 ug/ml, 5 days; 3-MA, 3-Methyladenine, 0.5 mM (**g**), Baf A1, bafilomycin A1, 4 μM (**h**). Data are presented as mean ± SEM. *P < 0.05; NS: not significant. Additional statistical details are provided in Supplementary Table 1.
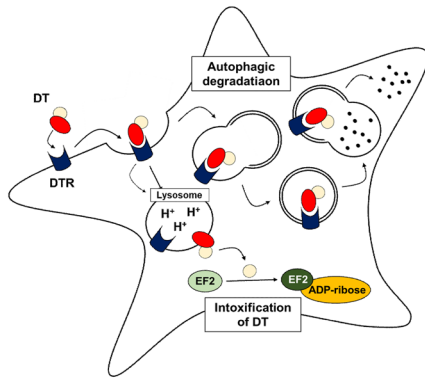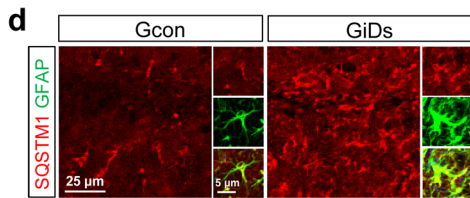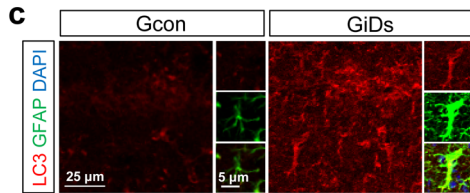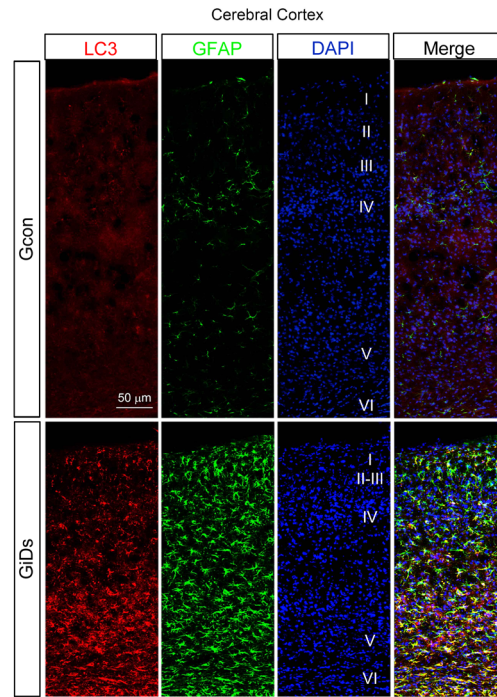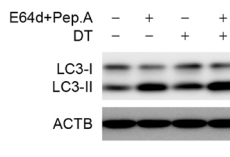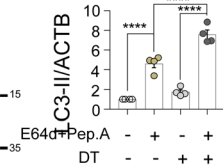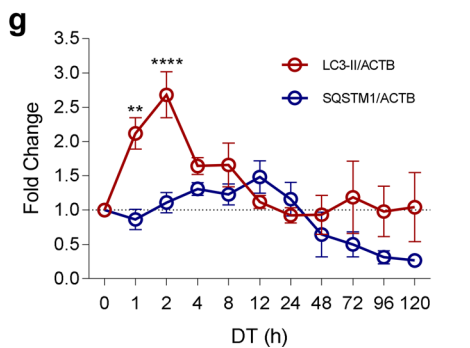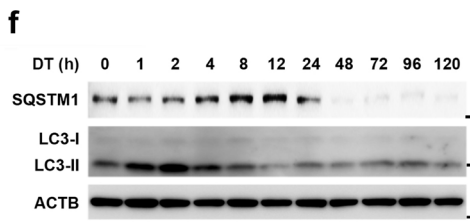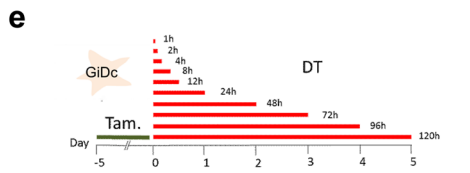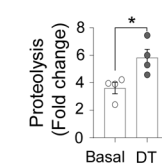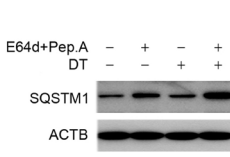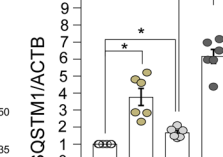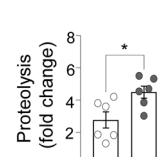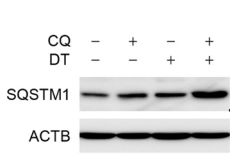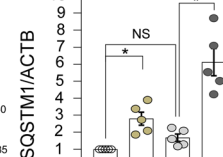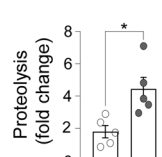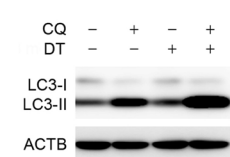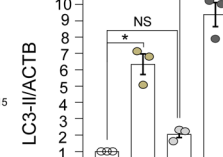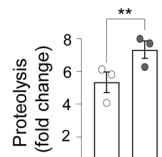
**Extended Data Fig. 2 |** See next page for caption.

Extended Data Fig. 2 | Autophagy activation in astrocytes of GiDs and GiDc. a, Schematic diagram for possible mechanism of DT intoxification in GiD. **b**, Immunostaining for LC3 and GFAP in cortex of Gcon and GiDs. **c, d**, Immunostaining for LC3 (**c**) and SQSTM1 (**d**) in hippocampus of Gcon and GiDs. **e**, Experimental timeline for DT treatment in cultured astrocytes from Gcon and GiD (GiDc). **f, g**, Western blot analysis showing that levels of endogenous SQSTM1 and LC3-II are time-dependently increased in DT-treated GiDc astrocyte. **h-s**, Autophagic flux assay and densitometry analysis in DT-treated GiDc astrocytes. DT, 1 µg/ml, 8 hrs; E64d+Pep.A, 10 µg/ml E64d plus 10 µg/ml Pep.A, 6 hrs (**h-m**); CQ, 20 µM, 6 hrs (**n-s**). Data are presented as mean ± SEM. *P < 0.05, **P < 0.01, ***P < 0.001, ****P < 0.0001; NS: not significant. Additional statistical details are provided in Supplementary Table 1.

a

b

c

d

e
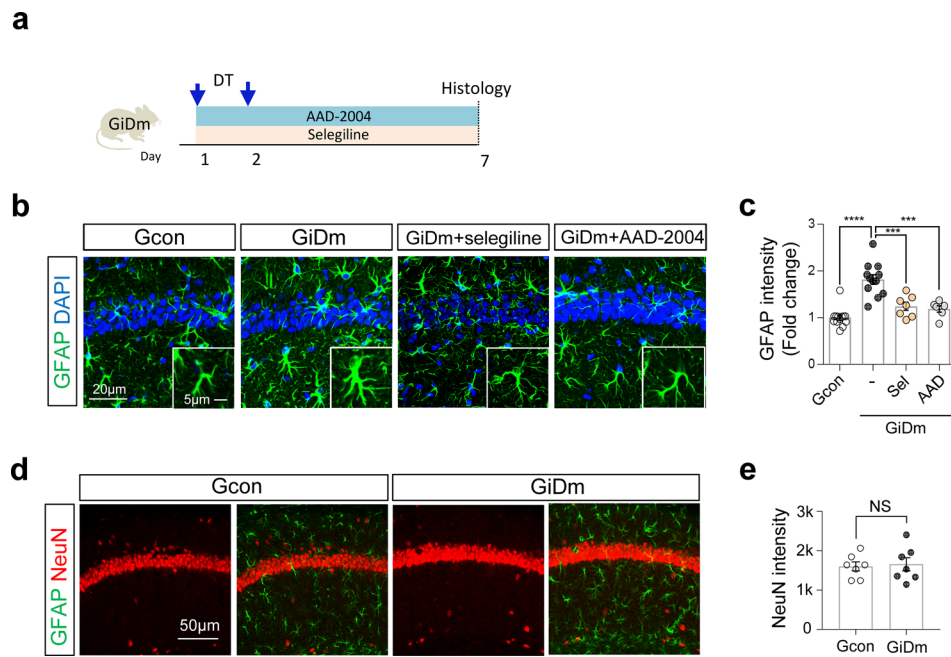
Extended Data Fig. 3 | MAO-B-mediated astrocytic hypertrophy and lack of neurodegeneration in GiDm brain. a, Experimental procedures for AAD-2004 and selegiline treatment in GiDm. **b,c**, Immunostaining and quantification for GFAP in Gcon, GiDm, selegline-treated GiDm and AAD-2004-treated GiDm. **d,e**, Immunostaining and quantification for NeuN in Gcon and GiDm. Data are presented as mean ± SEM. ***P < 0.001, ****P < 0.0001; NS: not significant. Additional statistical details are provided in Supplementary Table 1.

a
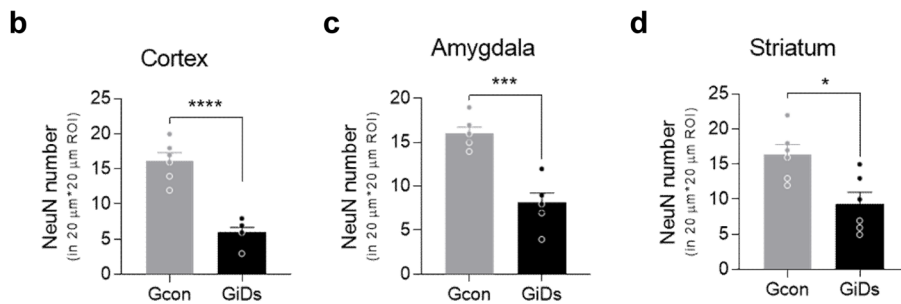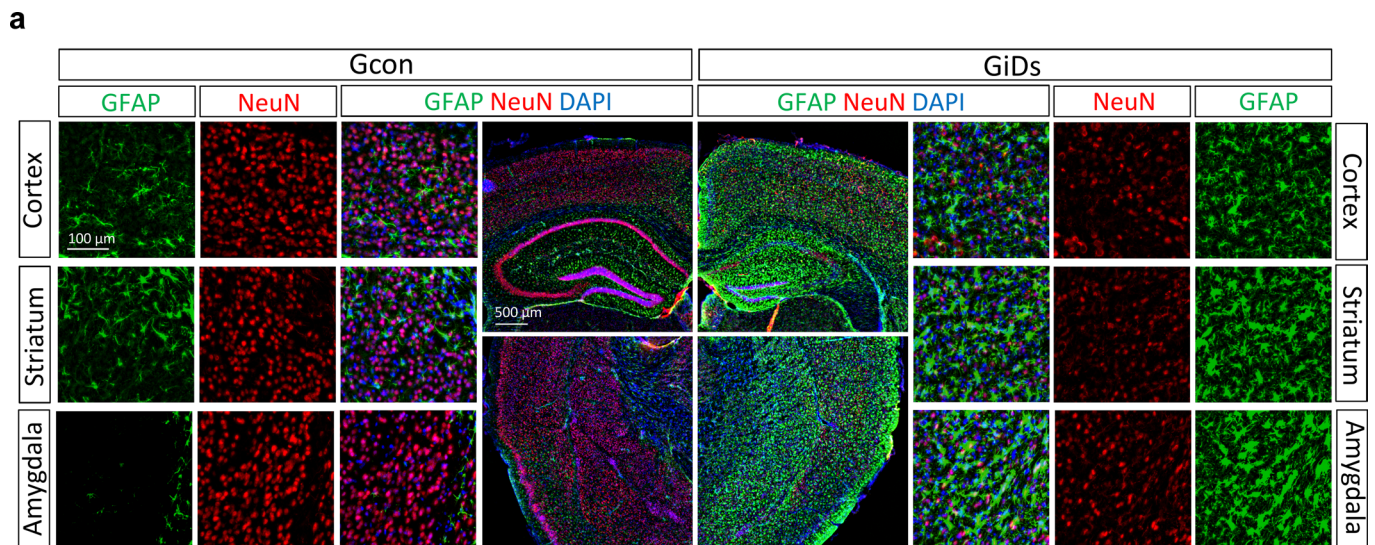
**Extended Data Fig. 4 | Astrocytic hypertrophy and neurodegeneration in cortex, striatum and amygdala of GiDs brain. a**, Representative image of immunostaining for GFAP and NeuN in the brain of Gcon and GiDs. **b-d**, Quantification for the number of cells positive for NeuN in cortex, striatum and amygdala of Gcon and GiDs. Data are presented as mean ± SEM. *P < 0.05, ***P < 0.001, ****P < 0.0001. Additional statistical details are provided in Supplementary Table 1.
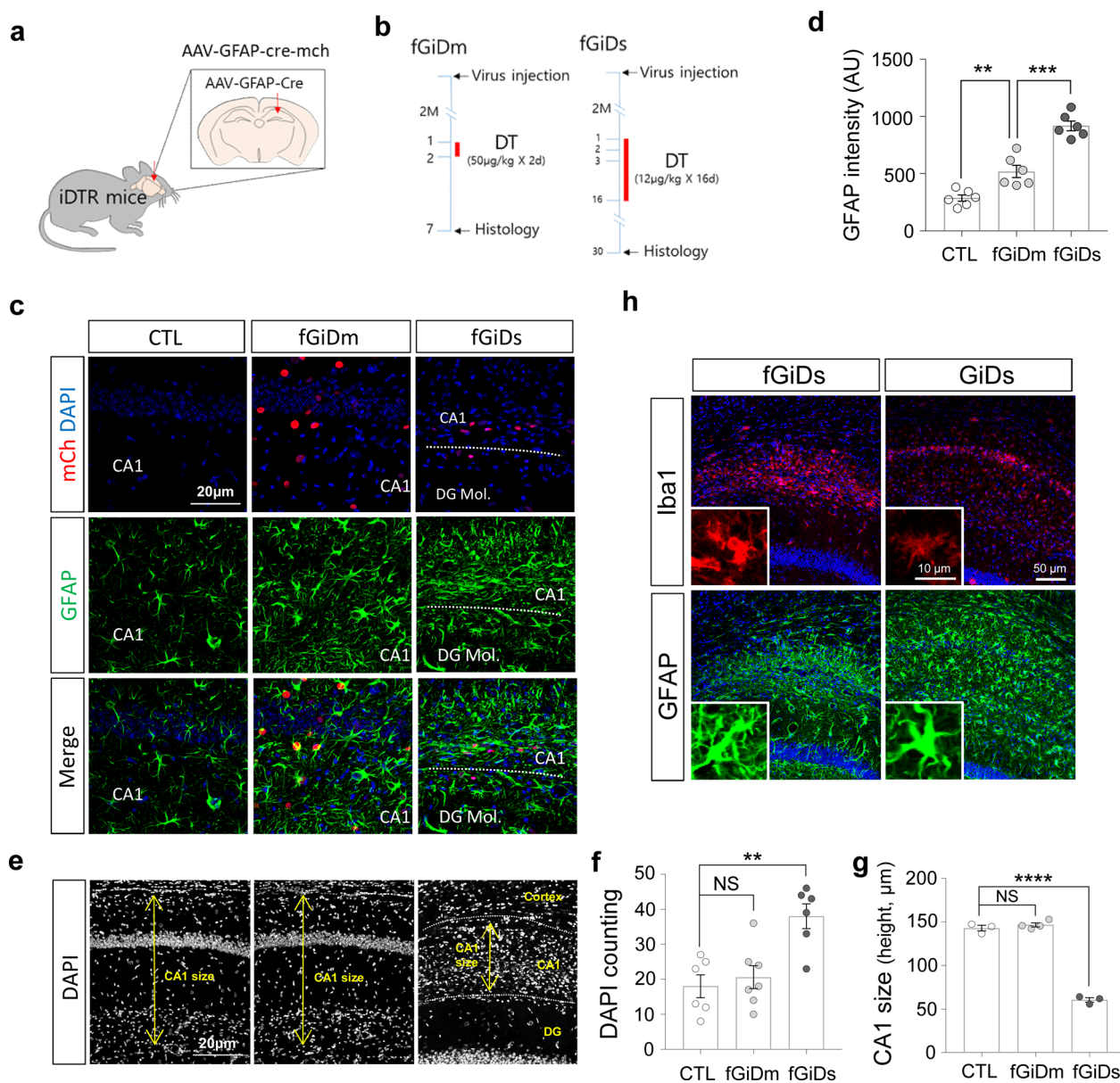
Extended Data Fig. 5 | Development of focal GiD (fGiD). a, **b**, Schematic diagram and experimental procedure for making mild and severe focal GiD, fGiDm and fGiDs, respectively. **c**, Immunostaining for GFAP and mCherry in CTL, fGiDm and fGiDs. **d**, Quantification for GFAP intensity in CTL, fGiDm and fGiDs. **e**, DAPI image in CTL, fGiDm and fGiDs. **f**, Counting the number of DAPI signals in stratum radiatum of CTL, fGiDm and fGiDs. **g**, Measuring the size of CA1 region in CTL, fGiDm and fGiDs. **h**, Comparison of glial activation in hippocampus between fGiDs and GiDs. Data are presented as mean ± SEM. **P < 0.01, ***P < 0.001, ****P < 0.0001; NS: not significant. Additional statistical details are provided in Supplementary Table 1.
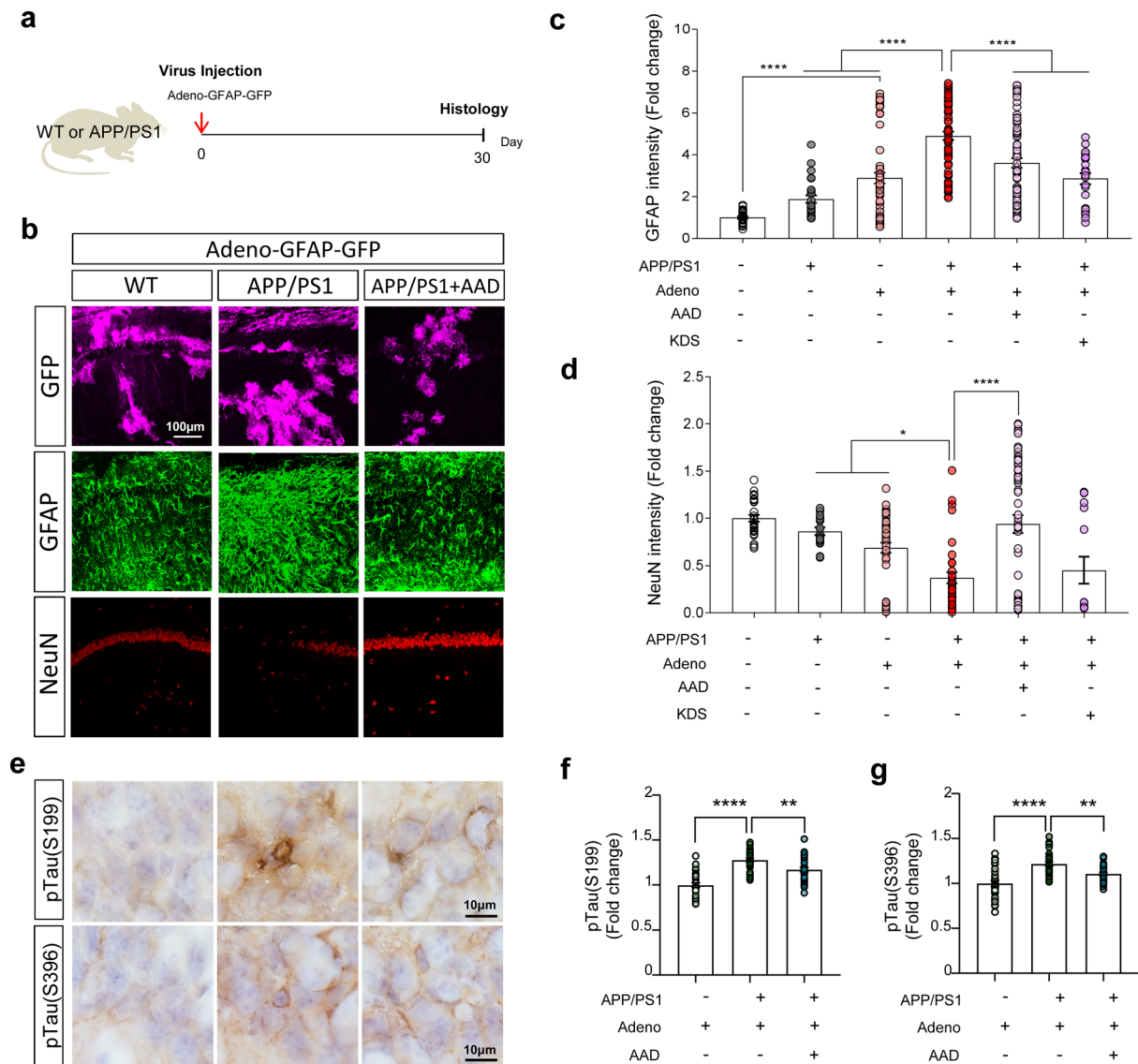
Extended Data Fig. 6 | Virus-mediated increase of astrocyte's reactivity and its effects on neurodegeneration and tauopathy in APP/PS1 mice. a, Schematic diagram and experimental timeline for increasing the reactivity of astrocytes in APP/PS1 mice using Adeno-GFAP-GFP virus. **b-d**, Immunostaining for GFAP, NeuN and quantification of the mean intensity in uninjected- or virus injected- WT and APP/PS1 mice. Magenta, Adeno-GFAP-GFP virus. **e-g**, DAB staining and quantification for p-Tau(S199) and p-Tau(S396) in virus injected- WT and APP/PS1 mice. Data are presented as mean ± SEM. *P < 0.05, **P < 0.01, ****P < 0.0001; NS: not significant. Additional statistical details are provided in Supplementary Table 1.

nature research

Corresponding author(s): C. Justin Lee, Hoon Ryu

Last updated by author(s): Oct 5, 2020

Reporting Summary

Nature Research wishes to improve the reproducibility of the work that we publish. This form provides structure for consistency and transparency in reporting. For further information on Nature Research policies, see our Editorial Policies and the Editorial Policy Checklist.

Statistics

For all statistical analyses, confirm that the following items are present in the figure legend, table legend, main text, or Methods section.

n/a	Confirmed	
☐	☒	The exact sample size (*n*) for each experimental group/condition, given as a discrete number and unit of measurement
☐	☒	A statement on whether measurements were taken from distinct samples or whether the same sample was measured repeatedly
☐	☒	The statistical test(s) used AND whether they are one- or two-sided *Only common tests should be described solely by name; describe more complex techniques in the Methods section.*
☐	☒	A description of all covariates tested
☐	☒	A description of any assumptions or corrections, such as tests of normality and adjustment for multiple comparisons
☐	☒	A full description of the statistical parameters including central tendency (e.g. means) or other basic estimates (e.g. regression coefficient) AND variation (e.g. standard deviation) or associated estimates of uncertainty (e.g. confidence intervals)
☐	☒	For null hypothesis testing, the test statistic (e.g. *F*, *t*, *r*) with confidence intervals, effect sizes, degrees of freedom and *P* value noted *Give P values as exact values whenever suitable.*
☒	☐	For Bayesian analysis, information on the choice of priors and Markov chain Monte Carlo settings
☒	☐	For hierarchical and complex designs, identification of the appropriate level for tests and full reporting of outcomes
☐	☒	Estimates of effect sizes (e.g. Cohen's *d*, Pearson's *r*), indicating how they were calculated

Our web collection on statistics for biologists contains articles on many of the points above.

Software and code

Policy information about availability of computer code

Data collection	We used ImageJ (NIH, version: 1.52s) to collect the data from immunohistochemistry. Imaging Workbench software and pCLAMP9.2 software were used for electrophysiological experiments.
Data analysis	We used Prism7 (GraphPad Software, Inc.) for statistical analysis.

For manuscripts utilizing custom algorithms or software that are central to the research but not yet described in published literature, software must be made available to editors and reviewers. We strongly encourage code deposition in a community repository (e.g. GitHub). See the Nature Research guidelines for submitting code & software for further information.

Data

Policy information about availability of data

All manuscripts must include a data availability statement. This statement should provide the following information, where applicable:
- Accession codes, unique identifiers, or web links for publicly available datasets
- A list of figures that have associated raw data
- A description of any restrictions on data availability

-We deposited the raw data and the statistics in a public repository, Mendeley (https://data.mendeley.com/), with accession code (DOI: 10.17632/8mf35ntz9z.1)
-The data that support the findings of this study are available from the corresponding author upon reasonable request.

Field-specific reporting

Please select the one below that is the best fit for your research. If you are not sure, read the appropriate sections before making your selection.

☒ Life sciences   ☐ Behavioural & social sciences   ☐ Ecological, evolutionary & environmental sciences

For a reference copy of the document with all sections, see nature.com/documents/nr-reporting-summary-flat.pdf

Life sciences study design

All studies must disclose on these points even when the disclosure is negative.

Sample size	No statistical method was used to predetermine sample size. Sample sizes were determined empirically based on our previous experiences or the review of similar experiments in literatures.
Data exclusions	Data were mostly excluded only on technical basis (e.g. unsuccessful surgery determined by mis-location of cannula or by virus expression in non-targeted area, software failure during behavioral data collection or faulty electrodes during recordings). Fig 2c: two data points were excluded after outlier test. Fig 5i, j: two data points in WT+DTR group and one data point in APP/PS1+DTR group were excluded for virus-mislocation.
Replication	All experiments in this study are representative of at least two biological replicates (mice or cell culture preparations) except for Extended Data Figure 2b-d (these are examined once).
Randomization	For GiD and APP/PS1 mice, mice with required genotypes were randomly assigned to the experimental groups and treated in the same way. Also, astrocytes culture preparations from mouse pups were randomly assigned to the experimental groups
Blinding	To perform behavioral experiments in a blinded manner, animal preparation, experiments and data analysis were performed by different investigators. On the other hand, for astrocyte culture experiment, data collection and analysis were not performed blind to the conditions of the experiments.

Reporting for specific materials, systems and methods

We require information from authors about some types of materials, experimental systems and methods used in many studies. Here, indicate whether each material, system or method listed is relevant to your study. If you are not sure if a list item applies to your research, read the appropriate section before selecting a response.

Materials & experimental systems

n/a	Involved in the study
☐	☒ Antibodies
☐	☒ Eukaryotic cell lines
☒	☐ Palaeontology and archaeology
☐	☒ Animals and other organisms
☐	☒ Human research participants
☒	☐ Clinical data
☒	☐ Dual use research of concern

Methods

n/a	Involved in the study
☒	☐ ChIP-seq
☒	☐ Flow cytometry
☒	☐ MRI-based neuroimaging

Antibodies

Antibodies used	For immunohistochemistry, primary antibodies used are as follow: Chicken anti-GFAP (Millipore, Cat. No. Ab5541), Rabbit anti-Iba1 (Wako, Cat. No. 019-19741), Mouse anti-NeuN (Millipore, Cat. No. MAB377), Guinia pig anti-GABA (Millipore, Cat. No. Ab175), Rabbit anti-LC3 (Novus Biologicals, Cat. No. NB100-2220), Rabbit anti-SQSTM1/p62 (Abcam, Cat. No. ab91526), Mouse anti-Ki67 (Novocstra, Cat. No. KI67-MM1-L-CE), Rabbit anti-ACTB/b-ACTIN (ROCKLAND, Cat. No. 600-401-886), Mouse anti-TUBB3/TUBULIN (Millipore, Cat. No. 05-559), Chicken anti-GFP (Abcam, Cat. No. Ab13970), Mouse anti-p67[phox] (BD Biosciences, Cat. No. 610913), Rabbit anti-iNOS/NOS type II (BD Biosciences, Cat. No. 610332), Mouse anti-Neurofilaments, phosphorylated (SMI31) (BioLegend, Cat. No. SMI-31R), Rabbit anti- Nitrotyrosine (Thermo Fisher Scientific, Cat. No. A21285), Rabbit anti-Tau (phospho S199) (Abcam, Cat. No. ab81268), Rabbit anti-Tau (phospho S396) (Abcam, Cat. No. ab109390), Mouse anti-pTau(S202/T205) (Thermo Fisher Scientific, Cat. No. MN1020), Mouse anti-GFAP (Neuromap, Cat. No. 75-240), and Mouse anti-Tuj1 (Cell Signaling Technology, Cat. No. NBP142568) antibodies, donkey anti-chicken-488 (Jackson, Cat. No. 703-545-155) and donkey anti-guinea pig-594 (Jackson 706-585-148). For western blotting, primary antibodies used are as follow: Rabbit anti-LC3 (Novus Biologicals, Cat. No. NB100-2220), Rabbit anti-SQSTM1/p62 (Abcam, Cat. No. ab91526) and Rabbit anti-ACTB/b-ACTIN (ROCKLAND, Cat. No. 600-401-886) antibodies, anti-rabbit HRP (Amersham, NIF824; Pierce, 170-6515), anti-rabbit HRP (Pierce, 170-6516)
Validation	Anti-GFAP(Millipore), anti-Iba1, anti-NeuN and anti-GABA was validated in our previous paper (Jo, et al., Nat. Med. 20, 886–896,

Validation	2014). Anti-GFP was validated in previous reports including Suberbielle, et al (Nat. Comm. 6, 8897, 2015). Anti-LC3, anti-SQSTM1/p62, anti-ACTB/b-ACTIN and anti-TUBB3/TUBULIN were validated in previous reports including Kim et al (Autophagy 11, 796, 2015). Anti-p67[phox] was validated in previous reports including Li et al (PNAS 102, 9936, 2005). Anti-iNOS/NOS type II was validated in previous reports including Baek et al (Mol Brain. 9, 99, 2016). Anti-Neurofilaments, phosphorylated (SMI31) was validated in previous reports including McLean et al (PLoS One. 9, e110174, 2014). Anti-Tau (phospho S199) and anti-Tau (phospho S396) was validated in previous reports including Kim et al (Scientific Reports, 5, 15231, 2015).

Eukaryotic cell lines

Policy information about cell lines

Cell line source(s)	ReN cell VM human neural progenitor cells (hNPCs) were purchased from EMD Millipore (Billerica, MA, USA)
Authentication	None of the cell lines used have been authenticated.
Mycoplasma contamination	All cell lines tested negative for mycoplasma contamination.
Commonly misidentified lines (See ICLAC register)	No commonly misidentified cell lines were used.

Animals and other organisms

Policy information about studies involving animals; ARRIVE guidelines recommended for reporting animal research

| Laboratory animals | The mice used in this study were of mixed sexes, and experimental groups contained a balance of female and male mice. We used 8~12 weeks age of GiD mice and 10~12 months age of APP/PS1 mice.
Transgenic mouse used are as follow: iDTR (The Jackson Laboratory, JAX: 007900), GFAP-CreERT2 (The Jackson Laboratory, JAX: 012849), CamK2a-Cre (The Jackson Laboratory, JAX: 005359), APPswe/PSEN1dE9 (APP/PS1) (The Jackson Laboratory, JAX: 34832), and B6.Cg-Gt(ROSA)26Sortm9(CAG-tdTomato)Hze/J (The Jackson Laboratory, JAX: 007909) |
|---|---|
| Wild animals | This study did not involve wild animals. |
| Field-collected samples | This study did not involve samples collected from the field. |
| Ethics oversight | All animal care and handling was performed according to the Institutional Animal Care and Use Committee of IBS (Daejeon, Korea) |

Note that full information on the approval of the study protocol must also be provided in the manuscript.

Human research participants

Policy information about studies involving human research participants

Population characteristics	Human postmortem cortex tissues were examined from Boston University's Alzheimer's Disease Center (BUADC) with and without cognitive impairment who underwent annual cognitive evaluations using the National Alzheimer's Disease Coordinating Center (NACC) Uniform Data Set (UDS) protocol. Consents for brain donation and research participation were provided by the donor's next of kin. Institutional review boards from the Boston University Medical Center approved brain donation, post-mortem clinical record review, neuropathological evaluation, and clinical interviews with donor family members. In cases of normal subjects, brain tissues with the Braak Stage of I to II were used for immunohistochemistry, qPCR, and RNA sequencing. In cases of AD patients, brain tissues with the Braak Stage of V to VI were used for immunohistochemistry, qPCR, and RNA-Seq.
Recruitment	We requested postmortem brain tissues from the brain banks that specimens could be above the age of 55 with a postmortem interval of less than 48 hours. All brain tissue samples were age and sex balanced between AD patients and controls.
Ethics oversight	Institutional review board approval for ethical permission was obtained through the BUADC. This study was reviewed by the Institutional Review Board of the Boston University School of Medicine (Protocol H-28974) and was approved for exemption because it only included tissues collected from post-mortem subjects not classified as human subjects.

Note that full information on the approval of the study protocol must also be provided in the manuscript.